Eulerian–Lagrangian simulations of shear thinning and shear thickening in suspensions of repulsive particles

Carl Dahmén ⓘ ; Christopher Ness ⓘ ; Luca Mazzei ✉ ⓘ

Check for updates

View Online

Export Citation

Related Content

Driven by Brownian motion Cox–Ingersoll–Ross and squared Bessel processes: Interaction and phase transition

Physics of Fluids (January 2025)

The new effect of oscillations of the total angular momentum vector of viscous fluid

Physics of Fluids (August 2022)

πάντα

ρεῖ

13 January 2026 18:06:05

Eulerian–Lagrangian simulations of shear thinning and shear thickening in suspensions of repulsive particles

Carl Dahmén,[1] Christopher Ness,[2] and Luca Mazzei[1,a)]

[1]*Department of Chemical Engineering, University College London, Torrington Place, London WC1E 7JE, UK*
[2]*School of Engineering, The University of Edinburgh, Edinburgh EH9 3FG, UK*

Abstract

Suspensions of neutrally buoyant, non-Brownian, repulsive particles dispersed in Newtonian fluids give rise to complex rheology, shear thinning at low shear rates and shear thickening at high shear rates. Despite extensive study, important aspects of their rheology remain in part unclear, including (i) the role of the drag force in the onset of shear thickening; (ii) the relation between the range of the repulsive force and the rate of shear thinning; and (iii) the value and shear rate dependence of the exponent describing their viscosity divergence. To address these questions, we study the rheology of these suspensions under simple shear flow via a comprehensive numerical Eulerian–Lagrangian model that resolves both the solid and liquid phases, thereby eliminating the need to prescribe the fluid velocity field. This approach allows us to test the assumption of ideal simple shear flow, where the phasic velocity profiles are linear and the shear rate is spatially uniform—an assumption that becomes increasingly inaccurate as the system approaches the jamming transition. Using a simple force balance and accounting for the drag-force hindrance function in the nondimensionalization of the shear rate, we retrieve the onset of shear thickening at the expected order of magnitude of dimensionless shear rate and obtain an expression for the interparticle equilibrium distance that fits the numerical results accurately. Treating the repulsive particles as apparent particles consisting of a rigid core and a soft shell, whose thickness is related to the interparticle equilibrium distance, we describe the suspension rheology by means of a modified Krieger–Dougherty equation, relating its parameters to the shear rate and the repulsive force range. © *2026 Author(s). All article content, except where otherwise noted, is licensed under a Creative Commons Attribution (CC BY) license (https://creativecommons.org/licenses/by/4.0/).* https://doi.org/10.1122/8.0000932

I. INTRODUCTION

Suspensions of non-Brownian, repulsive particles dispersed in Newtonian fluids exhibit a complex rheology characterized by shear thinning, shear thickening, and regions where their viscosity does not depend on the shear rate. Repulsive forces typically emerge from ions that accumulate around the particle surfaces, forming electric double layers. These forces decrease exponentially as the distance from the particle surface increases. Their magnitude and characteristic range (referred to as the Debye length) are influenced by material properties and ionic strength and play a key role in determining the suspension viscosity. For example, Jeffrey and Acrivos [1] observed that increasing the ionic strength can reduce the viscosity of a model suspension by several orders of magnitude. In many industrial processes, controlling the ionic strength is crucial to achieving the desired rheological performance. For instance, in the coating of catalytic converters [2], maintaining a low viscosity of the "washcoat" is critical.

In general, the suspension viscosity η_m is correlated with the solid volume fraction ϕ, the shear rate $\dot{\gamma}$, and the strength and range of the repulsive forces. Establishing this functional dependence would greatly facilitate process design and optimization. To achieve this by simulation, one must model the suspension dynamics, accounting for the repulsive forces, and extract rheological information via averaging [3]. To do so, the most suitable modeling approach is one that resolves the microscopic dynamics of individual particles and accurately captures all relevant particle-particle interactions, including those arising from repulsive forces. In contrast, a detailed description of the motion of the ambient fluid, at a length scale much smaller than the particle size, is unnecessary; here, a mean-field description suffices, where the fluid-particle interactions are modeled via appropriate closures. This leads to the unresolved Eulerian–Lagrangian modeling approach adopted in this work [4]. Although this approach does not yield the suspension stress tensor (and thus the rheology) directly, this can be obtained via a suitable averaging scheme—the same scheme used to model the solid phase as a continuum, resulting in the Eulerian–Eulerian description of the mixture dynamics [5].

In an *ideal* simple shear flow, where the fluid and solid phases have *the same* mean velocity and the shear rate and volume fraction are *spatially uniform*, a Eulerian–Lagrangian model is expected to give very similar predictions to those of simpler models in which a linear fluid velocity profile is prescribed [6–8]. However, at the jamming point, the particles are immobile and, as we will show, the fluid velocity profile is *highly nonlinear*, while near this transition point, jamming can arise locally and intermittently, producing nonlinear velocity profiles and *interphase slip* that can only be captured

---

a)Author to whom correspondence should be addressed; electronic mail: l.mazzei@ucl.ac.uk

when the fluid phase is resolved. Here, a Eulerian–Lagrangian model is valuable not only to describe the suspension dynamics more accurately but also to assess whether *globally averaged* properties of the suspension are physically meaningful.

Our model is developed within a computational fluid dynamics-discrete element method (CFD-DEM) framework and is implemented in the open-source software "CFDEM".[1] Based on the work of Jamshidi *et al.* [9], it differs from other CFD-DEM models in its interpretation of the fluid effective stress tensor, which accounts for the particle presence stress in line with the arguments advanced by Jackson [3], Zhang and Prosperetti [10], and Nott *et al.* [11], and in the way it closes the mean fluid-particle interaction force, accounting for the contribution of the lubrication forces, in line with the arguments advanced by Nott *et al.* [11] and Jamshidi *et al.* [9]. The CFD part of the model includes the locally averaged mass and linear momentum balance equations for the fluid phase and, thus, calculates (instead of assuming) the *locally averaged* velocity and shear rate fields of the fluid phase and in turn of the suspension.

In this work, we employ this model to study the rheology of suspensions of neutrally buoyant, repulsive particles in simple shear flow, but the model is of *general validity*. For example, it can be employed to study more complex flows such as those of a suspension around a solid body, in a porous medium or in a fluidized bed.

Suspension rheology is a rapidly advancing field, driven by recent progress in bridging particle-scale physics with macroscopic flow behavior [12,13]. A key rheological parameter is the jamming volume fraction, as the suspension viscosity depends strongly on how close the solid volume fraction is to it [14]. The Krieger–Dougherty equation is the expression most commonly used to describe this dependence [15]. The jamming transition is sensitive to various properties of the particles, such as the friction coefficient of their surfaces [16–22], their shape [23], and adhesion [24,25]. A key finding is that jamming is associated with a spanning network of particle contacts that establishes under shear conditions [26]. For example, in suspensions of repulsive particles, shear thickening stems from the transition of the low-viscosity rheology of frictionless particles, with a higher jamming volume fraction, to the high-viscosity rheology of frictional particles, with a lower jamming volume fraction [6,27,28]. The influence of the drag force on this transition, however, has been seldom discussed in the literature. Less well-understood is how particle properties influence the rates of shear thinning and of the viscosity divergence leading to jamming, described by the exponent in the Krieger–Dougherty (KD) equation. For instance, studies have shown that the viscosity of soft particle suspensions increases more abruptly near jamming, corresponding to a smaller KD exponent [29,30]. Therefore, in this work, we aim to investigate (i) the role of the drag force in the onset of shear thickening,

(ii) the relation between the range of the repulsive force and the rate of shear thinning, and (iii) the value and shear rate dependence of the exponent describing the suspension viscosity divergence.

The article is organized as follows. Section II introduces the Eulerian–Lagrangian model used to simulate the suspensions. Section III reports the closure equations, introduces the stress tensors of the solid phase and the suspension, and defines the suspension viscosity. Section IV presents the simulation parameters and briefly discusses some issues related to numerical stability. Section V investigates the physical mechanisms underlying the rheology of suspensions of repulsive particles and derives an expression predicting the rate of shear thinning. Section VI presents the simulation results for suspensions of nonrepulsive frictionless and frictional particles, analyzing their velocity profiles, and then examines suspensions of repulsive frictional particles with different Debye lengths. Section VII summarizes the conclusions of this work. The article includes two appendices: Appendix A derives a novel critical time step for overdamped systems, while Appendix B derives the drag force scale accounting for the hindrance function.

II. MODEL

Here, we present the CFD-DEM model used to simulate the suspensions. In what follows, the variables are defined locally, being functions of spatial position x and time t. For brevity, these dependencies are omitted.

A. Locally averaged equations of motion for the fluid

The locally averaged equations of motion for the fluid read

$$\partial_t(\varepsilon \rho_e) = -\partial_x \cdot \varepsilon \rho_e \langle u \rangle_e, \tag{1}$$

$$\partial_t(\varepsilon \rho_e \langle u \rangle_e) = -\partial_x \cdot \varepsilon \rho_e \langle u \rangle_e \langle u \rangle_e \\ - \partial_x \cdot \langle S \rangle_e + \varepsilon \rho_e g - n \langle f \rangle_p, \tag{2}$$

where $\varepsilon = 1 - \phi$ and ρ_e are the volume fraction and density of the fluid, respectively. The derivation of these equations can be found in the literature [3,9–11]. Angle brackets denote locally averaged properties. $\langle u \rangle_e$ is the average fluid velocity, $\langle S \rangle_e$ is the fluid effective stress tensor, g is the gravitational field, n is the particle number density, and $n \langle f \rangle_p$ is the force exerted by the fluid on the particles per unit volume of suspension.

The expression for the fluid effective stress tensor was derived through a rigorous averaging procedure by Jackson [3] and reads

$$\langle S \rangle_e \equiv \varepsilon \langle \sigma \rangle_e + n \langle A \rangle_p + \varepsilon \rho_e \langle \hat{u}\hat{u} \rangle_e, \tag{3}$$

where $\langle \sigma \rangle_e$ is the mean value of the point stress tensor of the fluid, while $\langle \hat{u}\hat{u} \rangle_e$ is the mean value of the dyadic product of the fluid velocity fluctuations. The first term on the right-hand side of Eq. (3) is present because, before the averaging is carried out, the liquid phase is already modeled as a fluid and, thus, is already endowed with a point stress tensor. The last term is a Reynolds stress type of contribution but is not necessarily related to turbulence [3,10,31,32]. The term

$n\langle A\rangle_p$ is related to the interaction between the fluid and the particles (through the stress forces exerted by the fluid on the particle surfaces) and is known as the particle-presence stress tensor [3,10,33]. This term is often regarded as part of the solid stress tensor; however, as discussed by Nott *et al.* [11] and Jamshidi *et al.* [9], doing so is incorrect. Following Jamshidi *et al.* [9], we divide this tensor into two parts,

$$n\langle A\rangle_p = n\langle A\rangle_p^\star + n\langle A\rangle_p^\bullet. \tag{4}$$

The starred term is related to the distortion of the fluid streamlines around the particles [32]. This term is always present and in dilute suspensions yields the Einstein correction for the mixture viscosity [34]. The second term is related to the lubrication forces between neighboring particles and becomes important in dense systems with $\phi \gtrsim 0.2$ [9]. Defining

$$\langle S\rangle_e^\star \equiv \varepsilon\langle\sigma\rangle_e + n\langle A\rangle_p^\star + \varepsilon\rho_e\langle\hat{u}\hat{u}\rangle_e, \tag{5}$$

we then obtain

$$\langle S\rangle_e = \langle S\rangle_e^\star + n\langle A\rangle_p^\bullet, \tag{6}$$

in which the first term on the right is always present, while the second term is significant only in dense suspensions.

B. Equations of motion for the solid particles

The equations of motion for each suspended particle read

$$m\dot{u}_r = f_r + \sum_s \left(f_{rs}^c + f_{rs}^i\right) + mg, \tag{7}$$

$$I\dot{\omega}_r = l_r + \sum_s \left(l_{rs}^c + l_{rs}^\bullet\right), \tag{8}$$

where m is the particle mass, $\dot{u}_r$ is the acceleration of particle r, f_r is the force exerted on particle r by the fluid (and includes the lubrication, drag, and buoyancy forces), while f_{rs}^c and f_{rs}^i are the forces exerted by particle s on particle r due to direct contact and short-ranged repulsion, respectively (for a given particle r, these forces are nonzero only for a small subset of neighboring particles s). Equation (8) is the balance equation for the angular momentum, where I is the moment of inertia of a particle about its center and $\dot{\omega}_r$ is the angular acceleration of particle r, while l_r, l_{rs}^c, and $l_{rs}^\bullet$ are, respectively, the torques acting on particle r generated by the fluid-particle interaction and by the direct contact and lubrication forces between particles r and s.

III. CLOSURE EQUATIONS

The balance equations presented in Sec. II are unclosed; thus, in their current form, they cannot be solved. In the linear momentum balance equation for the fluid, the unclosed terms are the fluid effective stress tensor $\langle S\rangle_e$ and the fluid-particle interaction force $n\langle f\rangle_p$, while in the equations of motion for the particles, the unclosed terms are the fluid-particle interaction force f_r, the contact and repulsive forces f_{rs}^c and f_{rs}^i, and their associated torques.

We start by considering $n\langle f\rangle_p$ and f_r. In Sec. III A, as it is usually done in the literature, we divide these forces in their main components: the buoyancy, drag, and lubrication forces; here, we also discuss the definition of buoyancy force, which for suspensions is not trivial. In Sec. III B, we then present the closures for the lubrication forces ($\varepsilon\partial_x \cdot n\langle A\rangle_p^\bullet$ and $f_{rs}^\bullet$) and the associated torques ($l_{rs}^\bullet$). In Sec. III C, we consider the closures for the drag forces, both for a single particle ($f_{d,r}$) and per unit volume of suspension ($n\langle f_d\rangle_p$) and for the associated torques (l_r). Subsequently, in Secs. III D and III E, we present the closures for the contact forces and torques (f_{rs}^c and l_{rs}^c) and for the repulsive forces (f_{rs}^i). In Sec. III F, we then consider the closures for the contributors to the effective stress tensor of the fluid ($\varepsilon\langle\sigma\rangle_e$, $n\langle A\rangle_e^\star$ and $n\langle A\rangle_p^\bullet$). Finally, in Sec. III G, we introduce the effective stress tensors of the solid phase and of the suspension, concluding by defining the suspension viscosity.

A. Fluid-particle interaction force

The fluid-particle interaction force $n\langle f\rangle_p$ in Eq. (2) arises from the gradients of the point velocity of the ambient fluid generated over the surface of the particles [3]. Similarly to the particle-presence stress [see Eq. (4)], this force is related to the stress forces acting on the particle surfaces and arising from the velocity gradients generated by the distortion of the fluid streamlines around the particles and to the lubrication forces between neighboring particles [9,31]; accordingly, we divide the force into two parts,

$$n\langle f\rangle_p = n\langle f\rangle_p^\star + n\langle f\rangle_p^\bullet, \tag{9}$$

the first term on the right being related to the distortion of the fluid streamlines and the second term to the lubrication forces between particle pairs.

The overall force $n\langle f\rangle_p$ includes several terms; one of these is the buoyancy force, which, for suspensions, can be defined in various ways [35,36]. Here, we adopt the definition favored by Jackson [35], relating it to the divergence of the fluid effective stress tensor,

$$n\langle f_b\rangle_p \equiv -\phi\partial_x \cdot \langle S\rangle_e = -\phi\partial_x \cdot \left(\langle S\rangle_e^\star + n\langle A\rangle_p^\bullet\right). \tag{10}$$

In general, $n\langle f\rangle_p^\star$ comprises several contributions, but for the system of interest here, the buoyancy and drag forces are dominant. Accordingly, we write

$$n\langle f\rangle_p^\star = -\phi\partial_x \cdot \langle S\rangle_e^\star + n\beta(\langle u\rangle_e - \langle u\rangle_p). \tag{11}$$

The first term on the right is the buoyancy force part related to the distortion of the fluid streamlines around the particles, and the second term is the drag force, with β being the drag coefficient for a single particle.

As shown in Nott *et al.* [11] and, more recently, in Jamshidi *et al.* [9], $n\langle f\rangle_p^\bullet$ is equal to

$$n\langle f\rangle_p^\bullet = -\partial_x \cdot n\langle A\rangle_p^\bullet. \tag{12}$$

This force, which vanishes in homogeneous suspensions (for $n\langle A\rangle_p^\bullet$ is spatially uniform), has been often neglected in the literature but plays a key role in driving shear-induced particle migration. From Eq. (10), $-\phi\partial_x\cdot n\langle A\rangle_p^\bullet$ can be interpreted as the part of the buoyancy force related to the lubrication forces between particle pairs.

Combining Eqs. (9), (11), and (12), we obtain

$$
n\langle f\rangle_p = -\phi\partial_x\cdot\langle S\rangle_e \\
+ n\beta(\langle u\rangle_e - \langle u\rangle_p) - \varepsilon\partial_x\cdot n\langle A\rangle_p^\bullet. \tag{13}
$$

The first term on the right-hand side represents the total buoyancy force, in line with Eq. (10).

The fluid-particle interaction force featuring in Eq. (7) reads

$$
f_r = -V_p\partial_x\cdot\langle S\rangle_e^\star + f_{d,r} + \sum_s f_{rs}^\bullet, \tag{14}
$$

where the first term on the right-hand side represents the part of the buoyancy force related to the distortion of the fluid streamlines, $f_{rs}^\bullet$ is the lubrication force, $f_{d,r}$ is the drag force, and V_p is the particle volume.

Note that if Eq. (14) is averaged, Eq. (13) is recovered [9]. More specifically, the average of $-V_p\partial_x\cdot\langle S\rangle_e^\star + f_{d,r}$ is $n\langle f\rangle_p^\star$ and that of $\sum_s f_{rs}^\bullet$ is $n\langle f\rangle_p^\bullet$ (for further details, refer to Jackson [3] and Jamshidi *et al.* [9]). This does confirm that the expression of the fluid-particle interaction force for a particle is consistent with that per unit volume of suspension.

Now that these forces have been split in their contributors, we can address the closure problem for each one of them: first, we consider the lubrication forces (Sec. III B) and then the drag forces (Sec. III C).

B. Lubrication force

To model the lubrication forces, we adopt the short-ranged and pairwise closure derived by Jeffrey and Onishi [37] and Jeffrey [38] and adapted by Cheal and Ness [7] for DEM simulations. The lubrication force exerted on particle r by particle s takes the following form:

$$
f_{rs}^\bullet = \eta_e\big\{\big[X_{11}^A k_{rs}k_{rs} + Y_{11}^A(\delta - k_{rs}k_{rs})\big]\cdot(u_s - u_r) \\
- Y_{11}^B(\omega_r \times k_{rs}) - Y_{21}^B(\omega_s \times k_{rs})\big\}, \tag{15}
$$

where η_e is the viscosity of the Newtonian ambient fluid, k_{rs} is the unit vector pointing from the center of particle r to the center of particle s, and δ is the identity tensor, while u_r and ω_r are the linear and angular velocities of particle r, respectively. The torque is given by

$$
l_{rs}^\bullet = -\eta_e\big[Y_{11}^B(u_s - u_r) \times k_{rs} + (\delta - k_{rs}k_{rs})\cdot(Y_{11}^C\omega_r + Y_{12}^C\omega_s)\big]. \tag{16}
$$

For the expressions of the scalar resistances X_{11}^A, Y_{11}^A, Y_{11}^B, Y_{21}^B, Y_{11}^C, and Y_{12}^C, refer to Cheal and Ness [7]. Note that these expressions do not feature any adjustable parameters.

The lubrication force modeled by Eq. (15) diverges at particle contact, but it is customary to truncate it for surface-to-surface distances smaller than about 0.1% of the particle radius.

The part of the particle-presence stress tensor related to the lubrication forces, featuring in Eq. (6), is given by [9],

$$
n\langle A\rangle_p^\bullet \equiv \frac{a}{V_a}\sum_r\sum_s k_{rs}f_{rs}^\bullet, \tag{17}
$$

where a is the particle radius and the two sums are over all the particles r and s present in the averaging region of volume V_a. This region must be large enough to contain several particles so that the average is statistically meaningful, but its characteristic size must be much smaller than the length scale characterizing the spatial variations of the mean fields so that such variations are correctly captured.

C. Drag force

In Eq. (14), the drag force exerted by the fluid on particle r is taken to be proportional to the difference between the mean velocity of the fluid and the velocity of particle r. So, we have

$$
f_{d,r} \equiv \beta(\langle u\rangle_e - u_r), \tag{18}
$$

where β is the drag force coefficient and u_r is the velocity of particle r. The volume averaged drag force for the fluid phase, featuring in Eq. (13), is given by

$$
n\langle f_d\rangle_p \equiv \frac{1}{V_a}\sum_r f_{d,r}, \tag{19}
$$

where the sum is over all particles r in the averaging volume. In the literature, there are various closures for β. Here, we use that by Di Felice [39], written consistently with the definition of buoyancy force used in Eq. (11),

$$
\beta = \left[(\pi a^2)\frac{1}{2}\rho_e|\langle u\rangle_e - \langle u\rangle_p|C_D(\mathrm{Re})\right]\varepsilon^{2-\chi}, \\
\chi = 3.7 - 0.65\exp\left[\frac{-(1.5 - \log_{10}\mathrm{Re})^2}{2}\right], \tag{20}
$$

where the mean velocity of the solid phase is defined as

$$
n\langle u\rangle_p \equiv \frac{1}{V_a}\sum_r u_r, \tag{21}
$$

and the Reynolds number Re and friction coefficient C_D are given, respectively, by

$$
\mathrm{Re} \equiv \frac{\varepsilon\rho_e|\langle u\rangle_e - \langle u\rangle_p|2a}{\eta_e}, \tag{22}
$$

$$
C_D = \left(0.63 + \frac{4.8}{\sqrt{\mathrm{Re}}}\right)^2. \tag{23}
$$

Equation (20) features the mean velocity of the solid phase, so β has the same value for all the particles contained in the averaging volume. This ensures that Eq. (19) yields the

correct expression for the mean drag force per unit volume of suspension featuring in Eq. (13),

$$n\langle \boldsymbol{f}_d \rangle_p = n\beta(\langle \boldsymbol{u} \rangle_e - \langle \boldsymbol{u} \rangle_p). \tag{24}$$

Note that Di Felice [39]'s closure does not contain any adjustable parameters and has been extensively validated in the literature. For instance, see Mazzei [40] and references therein.

In Eq. (8), for the term $\boldsymbol{l}_r$, we account solely for the rotational component of the drag force. At low Reynolds numbers, this is often modeled by the Stokes torque,

$$\boldsymbol{l}_r = 8\pi\eta_e a^3(\langle \boldsymbol{\omega} \rangle_e - \boldsymbol{\omega}_r), \tag{25}$$

where $\langle \boldsymbol{\omega} \rangle_e$ is the mean angular velocity of the fluid, given by the axial vector associated with the antisymmetric part of the gradient of the fluid mean velocity field. Many studies, such as those by Blais and Bertrand [4] and Liu *et al.* [41], disregard the Stokes torque. As shown by Bnà *et al.* [42], its influence is negligible for particles with diameters up to several tens of micrometers. In light of this, and after verifying that this term is indeed negligible for the systems herein considered, we have omitted it in our simulations.

D. Contact force

To model the contact forces between particles, we employ the spring-dashpot model [43]. Here, the (absolute) normal and tangential particle overlaps, δ^n and δ^t, respectively, together with the relative particle collision velocities in the normal and tangential directions, u_{rs}^n and u_{rs}^t, respectively, are used to calculate the normal and tangential parts of $\boldsymbol{f}_{rs}^c$, as well as the torque $\boldsymbol{l}_{rs}^c$. These are modeled as follows:

$$\boldsymbol{f}_{rs}^c = \boldsymbol{f}_{rs}^{c,n} + \boldsymbol{f}_{rs}^{c,t}, \tag{26}$$

$$\boldsymbol{f}_{rs}^{c,n} = -\left(k^n\delta^n + \eta^n u_{rs}^n\right)\boldsymbol{k}_{rs}, \tag{27}$$

$$\boldsymbol{f}_{rs}^{c,t} = -\left(k^t\delta^t + \eta^t u_{rs}^t\right)\boldsymbol{t}_{rs}, \tag{28}$$

$$\boldsymbol{l}_{rs}^c = a\boldsymbol{k}_{rs} \times \boldsymbol{f}_{rs}^{c,t}, \tag{29}$$

with

$$\boldsymbol{u}_{rs} \equiv \boldsymbol{u}_r - \boldsymbol{u}_s + a(\boldsymbol{\omega}_r + \boldsymbol{\omega}_s) \times \boldsymbol{k}_{rs}, \tag{30}$$

$$u_{rs}^n \equiv \boldsymbol{u}_{rs} \cdot \boldsymbol{k}_{rs}; \quad u_{rs}^t \equiv \boldsymbol{u}_{rs} \cdot \boldsymbol{t}_{rs}. \tag{31}$$

Here, $\delta^t\boldsymbol{t}_{rs}$ denotes the incremental tangential displacement, reset at the initiation of each contact, while k and η are the spring and damping coefficients, respectively. The tangential force is truncated to fulfill Coulomb's law of friction $|\boldsymbol{f}_{rs}^{c,t}| \leq \mu|\boldsymbol{f}_{rs}^{c,n}|$, where μ is the friction coefficient. The tangential dashpot has no physical significance and is primarily used in granular media simulations as an efficient numerical stabilizer. Following Mari *et al.* [6], we omit tangential damping. For sufficiently hard particles, the absolute value of the spring coefficient does not affect the magnitude of the collision forces (see discussion in Sec. IV). The normal spring

coefficient is calculated from the material properties,[2]

$$k^n = \frac{16}{15\sqrt{2}}\sqrt{a}Y^\star\left(\frac{15\sqrt{2}mv_{ch}^2}{32\sqrt{a}Y^\star}\right)^{1/5}, \tag{32}$$

while the normal damping coefficient is given by

$$\eta^n = \frac{2mk^n}{1 + \left(\frac{\pi}{\ln e}\right)^2}, \tag{33}$$

where v_{ch} is a parameter that should reflect the characteristic impact velocity between particle pairs, but whose value is often set to fine-tune the normal spring coefficient, and e is the restitution coefficient (equal to unity for elastic particle collisions). The material property $Y^\star$ is defined as

$$Y^\star \equiv \frac{Y}{2(1 - \nu^2)}, \tag{34}$$

where Y and ν are the Young modulus and the Poisson ratio, respectively. The tangential spring coefficient is set equal to the normal one ($k^t = k^n$).

E. Repulsive force

We use a repulsive force similar to the electrostatic double layer force,

$$\boldsymbol{f}_{rs}^i = -F_0 e^{-(h-\delta_{rs})\kappa}\boldsymbol{k}_{rs}, \tag{35}$$

where F_0 is the force at contact, h is the interparticle surface distance, and κ^{-1} is the Debye length. δ_{rs} denotes the sum of the widths of the asperities for particles r and s; for $h \leq \delta_{rs}$, the force $\boldsymbol{f}_{rs}^i$ is set to be constant and equal to $-F_0\boldsymbol{k}_{rs}$. The theoretical Debye length is given by [44]

$$\kappa^{-1} = \left[\frac{\varepsilon_e\varepsilon_0\hbar T}{2q^2E}\right]^{1/2}, \tag{36}$$

where E is the ionic strength, q is the electric charge, ε_0 is the permittivity of vacuum, ε_e is the relative dielectric constant of the liquid, $\hbar$ is the Planck constant, and T is the absolute temperature. For typical values of E, Eq. (36) yields a Debye length between 1 and 10 nm, but in the literature far greater values have been considered (Mewis and Wagner [45], Chatté *et al.* [46], and Mari *et al.* [6]); here, we make the Debye length range between $0.0005a$ [order of magnitude given by Eq. (36)] and $0.05a$ (order of magnitude in the cited articles).

F. Effective stress of the fluid

As shown in Eq. (6), the fluid effective stress tensor $\langle \boldsymbol{S} \rangle_e$ is given by the sum of the tensors $\langle \boldsymbol{S} \rangle_e^\star$ and $n\langle \boldsymbol{A} \rangle_p^\bullet$. The latter is related to the lubrication forces, and therefore, its closure

---

[2]LAMMMPS improved for general granular and granular heat transfer simulations," retrieved from http://www.liggghts.com (2011).

was discussed in Sec. III B [see Eq. (17)]. The former, as shown in Eq. (5), involves two non-negligible terms: $\varepsilon\langle\boldsymbol{\sigma}\rangle_e$ and $n\langle\boldsymbol{A}\rangle_p^\star$ ($\varepsilon\rho_e\langle\hat{\boldsymbol{u}}\hat{\boldsymbol{u}}\rangle_e$ is insignificant for the flow considered here [3]). The former is the averaged fluid point stress tensor; its closure was rigorously derived by Joseph *et al.* [47] and reads

$$\varepsilon\langle\boldsymbol{\sigma}\rangle_e = \varepsilon\langle p\rangle_e\boldsymbol{\delta} - \eta_e\langle\dot{\boldsymbol{\gamma}}\rangle_v, \qquad (37)$$

where $\langle p\rangle_e$ is the fluid mean pressure, while $\langle\dot{\boldsymbol{\gamma}}\rangle_v$ is twice the deformation rate tensor of the following velocity field:

$$\langle\boldsymbol{u}\rangle_v \equiv \varepsilon\langle\boldsymbol{u}\rangle_e + \phi\langle\boldsymbol{u}\rangle_p. \qquad (38)$$

When the slip velocity between the fluid and solid phases is negligible, $\langle\dot{\boldsymbol{\gamma}}\rangle_v$ coincides with $\langle\dot{\boldsymbol{\gamma}}\rangle_e$, the latter denoting twice the deformation rate tensor for the fluid phase (i.e., of the velocity field $\langle\boldsymbol{u}\rangle_e$). Since this is the case of interest in our work, henceforth in Eq. (37), we replace $\langle\dot{\boldsymbol{\gamma}}\rangle_v$ with $\langle\dot{\boldsymbol{\gamma}}\rangle_e$. But note that in the CFD code, we implemented Eq. (37) in its general form. As we see, Eq. (37) features no adjustable parameters.

A closure for $n\langle\boldsymbol{A}\rangle_e^\star$ has been derived for dilute systems; for suspensions with solid volume fraction up to 5%, the equation derived by Jackson [3] holds,

$$n\langle\boldsymbol{A}\rangle_e^\star = \phi\langle p\rangle_e\boldsymbol{\delta} - \eta_e(5/2)\phi\langle\dot{\boldsymbol{\gamma}}\rangle_e. \qquad (39)$$

Hence, combining Eqs. (5), (37), and (39) gives

$$\langle\boldsymbol{S}\rangle_e^\star = \varepsilon\langle\boldsymbol{\sigma}\rangle_e + n\langle\boldsymbol{A}\rangle_e^\star = \langle p\rangle_e\boldsymbol{\delta} - \eta_m\langle\dot{\boldsymbol{\gamma}}\rangle_e \qquad (40)$$

where η_m is the mixture viscosity with Einstein correction,

$$\eta_m = \eta_e[1 + (5/2)\phi]. \qquad (41)$$

Equation (40) has been extended to higher volume fractions of solid, with the "Batchelor-Green" (BG) viscosity given by [48]

$$\eta_m = \eta_{BG} \equiv \eta_e[1 + D\phi + F\phi^2]. \qquad (42)$$

We adopt the coefficients suggested by Batchelor and Green [49], taking the Einstein coefficient $D = 2.5$ and $F = 7.6$. Notice that Eq. (42) predicts the mixture viscosity up to $\phi \approx 0.2$ [13,50]. For denser suspensions, Eqs. (40) and (42) are not sufficient, and other viscosity contributions, in particular that related to the lubrication forces, must be accounted for. This is done by considering the term $n\langle\boldsymbol{A}\rangle_p^\bullet$, that is, the second term on the right-hand side of Eq. (6), which represents the part of the particle-presence stress associated with the lubrication forces. In our CFD-DEM model, this term requires no closure because it can be calculated via Eq. (17).

G. Suspension properties

CFD-DEM models do not directly yield the stress tensors of the solid phase and the suspension; however, they provide all the information required to obtain them through averaging. The expression of the solid stress tensor is [3,36]

$$\langle\boldsymbol{S}\rangle_p \equiv n\langle\boldsymbol{B}\rangle_p^c + n\langle\boldsymbol{B}\rangle_p^i + \phi\rho_p\langle\hat{\boldsymbol{u}}\hat{\boldsymbol{u}}\rangle_p, \qquad (43)$$

where ρ_p is the density of the particles. The last term on the right-hand side of Eq. (43) is the kinetic stress tensor, which is related to the particle velocity fluctuations, and is negligible for the flow considered here [31]. $n\langle\boldsymbol{B}\rangle_p^c$ and $n\langle\boldsymbol{B}\rangle_p^i$ are the parts of the stress arising from direct particle contacts and repulsive interactions, respectively,

$$n\langle\boldsymbol{B}\rangle_p^c \equiv \frac{a}{V_a}\sum_r\sum_s\boldsymbol{k}_{rs}\boldsymbol{f}_{rs}^c, \qquad (44)$$

$$n\langle\boldsymbol{B}\rangle_p^i \equiv \frac{a}{V_a}\sum_r\sum_s\boldsymbol{k}_{rs}\boldsymbol{f}_{rs}^i, \qquad (45)$$

where $\boldsymbol{f}_{rs}^c$ and $\boldsymbol{f}_{rs}^i$ represent the contact and repulsive forces between particles r and s, respectively.

Now, if the interphase slip velocity is small, the suspension stress tensor is given by [5]

$$\langle\boldsymbol{S}\rangle_m \equiv \langle\boldsymbol{S}\rangle_e + \langle\boldsymbol{S}\rangle_p. \qquad (46)$$

The viscosity is obtained by modeling the suspension as a generalized Newtonian fluid, whereby

$$\eta_m \equiv \left|\frac{\langle\boldsymbol{\tau}\rangle_m : \langle\dot{\boldsymbol{\gamma}}\rangle_m}{\langle\dot{\boldsymbol{\gamma}}\rangle_m : \langle\dot{\boldsymbol{\gamma}}\rangle_m}\right|, \qquad (47)$$

where $\langle\boldsymbol{\tau}\rangle_m$ is the deviatoric part of $\langle\boldsymbol{S}\rangle_m$, while $\langle\dot{\boldsymbol{\gamma}}\rangle_m$ is twice the rate of deformation tensor of the suspension velocity field. η_m depends on the shear rate, which is defined as

$$|\langle\dot{\boldsymbol{\gamma}}\rangle_m| \equiv [(1/2)\langle\dot{\boldsymbol{\gamma}}\rangle_m : \langle\dot{\boldsymbol{\gamma}}\rangle_m]^{1/2}. \qquad (48)$$

Note that $\langle\boldsymbol{\tau}\rangle_m$ and $\langle\dot{\boldsymbol{\gamma}}\rangle_m$ are locally averaged variables; thus, Eq. (47) yields a *viscosity field*.

The balance equations for both phases with all the required closures, in their final form as implemented in the numerical code, are summarized in the supplementary material.

IV. SIMULATION CAMPAIGN

We simulate a 3D shear flow with periodic boundaries in the flow (x) and vorticity (y) directions and two planar walls normal to the gradient (z) direction. The bottom wall is fixed, while the top one moves horizontally at velocity $\dot{\gamma}L_z$, where $\dot{\gamma}$ is the *nominal* shear rate, while L_z is the distance between the walls (see Fig. 1). To ensure scale separation, L_z is two orders of magnitude larger than the particle radius a, while along the periodic directions, the separation-of-scales condition is not as strict, with L_x^p and L_y^p set equal to about $50a$. The key particle properties are the radius a, density ρ_p, normal stiffness k^n, and friction coefficient μ.
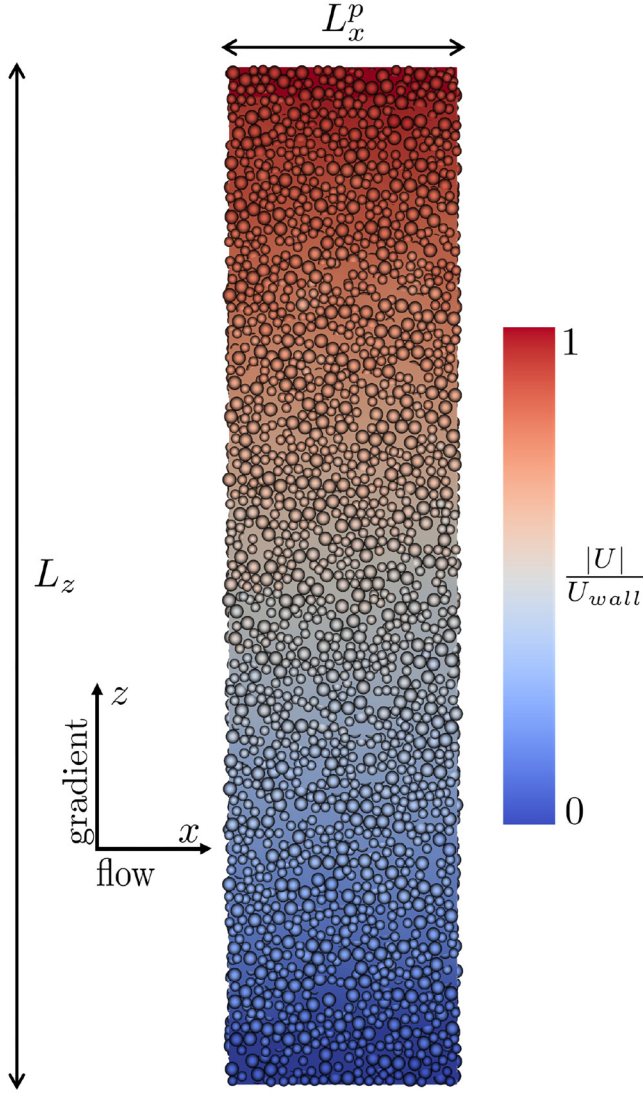
FIG. 1. Snapshot of the simulation setup showing the fluid and particle velocity fields under steady-state conditions with nonrepulsive particles at $\phi = 0.55$. The particles are colored according to the velocity magnitude scale; the background color is the fluid velocity field.

The fluid and particle phases are simulated separately with their own time steps, and at a given interval, they are coupled and exchange forces [4]. Both the fluid and particle time steps are critical for a stable and accurate simulation. There is a regime of particle time steps where the simulation is stable but generates unphysically large relative particle velocities. To address this issue, we derived a new time step criterion specifically for overdamped systems, accounting for the lubrication forces (see Appendix A). To ensure physically realistic simulations, the following quantities must be significantly smaller than unity:

$$\text{(i)} \, a/L_z \quad \text{(ii)} \, \rho_p \dot{\gamma} a^2/\eta_e \quad \text{(iii)} \, 6\pi\eta_e a\dot{\gamma}/k^n$$

$$\text{(iv)} \, \frac{\sqrt{\left[(3/2)\pi a^2 \eta_e/\delta\right]^2 + 4mk^n} - (3/2)\pi a^2 \eta_e/\delta}{\Delta t_D k^n}. \quad (49)$$

Condition (i) ensures the separation of scales between the size of the particles and the size of the flow domain, allowing us to model the solid phase as a continuum and guaranteeing bulk conditions. For our system, $a/L_z \sim 10^{-2}$.

Condition (ii) ensures that the inertia of the particles (and of the ambient fluid, since the particles are neutrally buoyant) is negligible. For our system, $\rho_p \dot{\gamma} a^2/\eta_e \sim 10^{-2}$.

Condition (iii) ensures that the particles are essentially rigid. Let us clarify the importance of this condition. In this work, our aim is to study the rheology of repulsive rigid particles; however, in our DEM model, the contact forces between the particles are elastic. This introduces in the model the force scale $k^n a$, which would be absent for strictly rigid particles. The relative importance between the drag force and the elastic force, quantified by the dimensionless number $6\pi\eta_e a\dot{\gamma}/k^n$, would introduce a shear-rate dependence of the suspension viscosity. To eliminate this effect and preserve the shear-rate independent behavior of rigid particles, we select a value for k^n that renders $6\pi\eta_e a\dot{\gamma}/k^n$ much smaller than unity, ensuring that the suspension is always in the asymptotic regime of nearly rigid particles. For our system, $6\pi\eta_e a\dot{\gamma}/k^n \sim 10^{-7}$.

Condition (iv) ensures a physical and stable simulation, where Δt_D is the DEM time step, $\delta/2$ is the width of the particle asperities, and m is the mass of a particle. For our system, the order of magnitude of this dimensionless number is 10^{-7}. Additionally, we introduced bidispersity to inhibit the formation of ordered phases observed in dense suspensions consisting of particles of the same size under shear. We chose a size ratio of $a_2/a_1 = 1.4$ [51], the two particle classes having the same volume fraction. Since the suspension is bidisperse, when we refer to the radius and width of the surface asperity, we take $a = \sqrt{a_1 a_2}$ and $\delta/2 = \sqrt{\delta_1\delta_2/4}$.

These conditions ensure that under constant friction (μ) and steady-state conditions, the viscosity η_r is a function only of the volume fraction ϕ. Adding repulsive interparticle forces to the system is thus the only force scale that can introduce a shear rate dependence for the mixture viscosity.

The equations from Secs. II and III are implemented in CFDEM, an extension of the CFD software OpenFOAM and the DEM software LIGGGHTS. The model parameters are summarized in Table I. To calculate the locally averaged variables, one must consider a volume of average containing a statistically significant number of particles but sufficiently smaller than the length scale over which the mean fields vary. In our model, the volume of average coincides with the CFD cell. Its volume is 3.2×10^{-5} mm^3, so for a solid volume fraction of 0.55, the cell contains roughly 20 particles. Moreover, in the velocity gradient direction, the computational grid comprises 33 CFD cells. Thus, the separation-of-scales condition is satisfied. Finally, to calculate the local solid volume fraction, we use the "divided approach" of Blais *et al.* [52].

In the figures reporting η_r against the shear rate presented in Sec. VI, η_r is obtained by averaging Eq. (47) over the entire flow domain. The mixtures are simulated over 50 units of strain ($\dot{\gamma}t$), with η_r averaged over the last 30 units.

Figure 1 shows a snapshot of the simulation, where L_z is the vertical length in the direction of the velocity gradient and L_x^p is the (periodic) horizontal length in the flow

TABLE I. Simulation parameters. x is the flow direction, z is the velocity gradient direction, and y is the neutral direction. The flow is periodic in the x and y directions.

Quantity	Symbol	Unit	Value
System geometry	$L_x^p \times L_y^p \times L_z$	mm	$0.23 \times 0.23 \times 1$
CFD cells	$N_x \times N_y \times N_z$	…	$7 \times 7 \times 33$
Fluid viscosity	η_e	Pa s	1×10^{-3}
Fluid density	ρ_e	kg/m³	1×10^3
Type 1 - radius	a_1	μm	5
Type 2 - radius	a_2	μm	7
Particle density	ρ_p	kg/m³	1×10^3
Type 1 - asperity width	$\delta_1/2$	nm	2.5
Type 2 - asperity width	$\delta_2/2$	nm	3.5
Top wall velocity (x)	U_{wall}	m/s	0.5
Debye length	κ^{-1}	nm	250, 125, 25, 2.5
Friction coefficient	μ	…	1
Young's modulus	Y	Pa	3×10^8
Poisson ratio	ν	…	0.3
Restitution coefficient	e	…	0.9
Characteristic velocity	v_{ch}	m/s	100
CFD time step	Δt_C	s	10^{-7}
DEM time step	Δt_D	s	10^{-8}
Boundary conditions	…	…	No slip/Periodic

direction. A velocity difference between the horizontal walls, U_{wall}, imposes a nominal shear rate of $\dot{\gamma} = U_{wall}/L_z$.

Besides the parameters characterizing the fluid (ρ_e, η_e), the particles (ρ_p, a_r, δ_r), and the repulsive force (F_0, κ), the model features seven parameters: D, F, Y, ν, e, v_{ch}, and μ. The first two are set equal to those obtained by Batchelor and Green [49] for suspensions of non-Brownian particles, while Y and ν are the Young modulus and the Poisson ratio, respectively. e is the restitution coefficient of the particles, v_{ch} is a parameter used to fine-tune the normal spring coefficient, and μ is the friction coefficient of the particles. Thus, the model features only two adjustable parameters: v_{ch} is primarily used to ensure that the particles are essentially rigid (condition iii), while μ is used to tune the jamming volume fraction and in turn the divergence of the suspension viscosity with the solid volume fraction.

V. A SIMPLE PHYSICAL MODEL

We now introduce a minimal physical model that captures the key features of the investigated system. This model will be valuable for interpreting the simulation results.

A. Newtonian rheology

Consider a pair of nonrepulsive particles in a suspension undergoing simple shear flow. Particle 1 is fixed relative to the coordinate system, while particle 2 approaches with a velocity of order of magnitude $\dot{\gamma}a$. In the Stokesian limit, where inertia is negligible, the drag force balances the lubrication force,

$$6\pi\eta_e a(\dot{\gamma}a - v)\varepsilon^{-3.70} \sim (3/2)\pi a^2\eta_e(v/h), \quad (50)$$

where h is the interparticle surface distance, v is the relative particle velocity, and the symbol $\sim$ means equality in the

order of magnitude. The left-hand side describes the order of magnitude of the drag force and includes the hindrance function, $\varepsilon^{-3.70}$, which previous works have omitted. The justification for its inclusion is detailed in Appendix B. Here, we point out that, although the focus is on two particles, these are part of a suspension, and the drag force acting on particle 2 is affected by the surrounding particles. The right-hand side describes the order of magnitude of the lubrication force and represents a simplified form of Eq. (15).

As the particles approach, particle 2 decelerates due to the lubrication force, v reduces, and the drag force rises, pushing the particles closer. Assuming that the lubrication film breaks down at a given cut-off length, the particles will always collide in a finite time. For rigid, non-Brownian, nonrepulsive particles in the Stokesian regime, the only force scale is the fluid dynamic one; thus, the suspension rheology is Newtonian regardless of friction. Its viscosity increases with ϕ, diverging at the jamming volume fraction ϕ_j. To characterize this relationship, the most widely used expression for the relative viscosity (normalized by the ambient fluid viscosity η_e) is the Krieger–Dougherty (KD) power law,

$$\eta_r = C(1 - \phi/\phi_j)^{-\lambda}. \quad (51)$$

C and λ are empirical constants, and to retrieve the Einstein [34] viscosity correction, these must be set to 1 and 2.5, respectively. Due to the number of degrees of freedom constrained at each contact point, networks of frictionless particles do not resist the flow to the same degree as networks of frictional particles, so the former can accommodate a larger ϕ before jamming. Frictionless suspensions generally have $\phi_j \approx 0.64$, while frictional ones have smaller jamming points, in some cases reported to be as low as $\phi_j \approx 0.57$ [12], with larger values having been reported in the literature [13,53].

B. Shear-thickening rheology

In suspensions of repulsive particles, shear thickening stems from the transition between the low-viscosity rheology of frictionless particles, which jam at higher volume fractions, and the high-viscosity rheology of frictional particles, which jam at lower volume fractions [27,28]. This transition is often marked by a critical stress $\sigma^\star$ that quantifies the repulsive stress magnitude, with $\sigma^\star$ taken equal to $F_0/6\pi a^2$ [6,19]. Shear thickening is expected to start when the dimensionless shear stress $\sigma/\sigma^\star$ has unit order of magnitude, a fact confirmed by experimental evidence. A critical shear rate has been used less often to characterize this transition, and the influence of the drag force has been rarely addressed. Here, we consider this alternative point of view and highlight the role of the drag force.

In a simple shear flow of a suspension of repulsive particles, two forces characterize the system: the drag force, induced by the applied shear, and the repulsive force. The scale (that is, the maximum value) of the former is $6\pi\eta_e a^2\dot{\gamma}\varepsilon^{-3.70}$, a value that corresponds to the absence of relative motion between the pair of particles considered in Sec. V A (in this case, the lubrication force is zero); the scale

of the latter is F_0. At low shear rates, the repulsive force dominates, so the particles do not come into direct contact and behave as frictionless particles. Conversely, at high shear rates, the drag force prevails, so the particles come into direct contact and behave as frictional particles. Shear thickening begins at the transition between the two states, when the scales of the two forces are equal. Hence, the characteristic shear rate is

$$\dot{\gamma}^\star \equiv \frac{F_0}{6\pi\eta_e a^2 \varepsilon^{-3.70}}. \tag{52}$$

The transition between the two states—and thus the increase in viscosity—is gradual. As $\dot{\gamma}$ approaches and then exceeds $\dot{\gamma}^\star$, the number of particles entering direct frictional contact grows progressively, leading to a corresponding gradual increase in viscosity and thus to shear thickening. The viscosity always follows Eq. (51); however, for $\dot{\gamma}/\dot{\gamma}^\star \ll 1$, ϕ_j corresponds to the jamming volume fraction of frictionless particles, whereas for $\dot{\gamma}/\dot{\gamma}^\star \gg 1$, ϕ_j corresponds to the jamming volume fraction of frictional particles. In this second limit, the repulsive force is negligible compared with the drag force, and the viscosity is independent of the shear rate.

In what follows, we plot the rheology data as a function of $\dot{\gamma}/\dot{\gamma}^\star$ and find that, as expected, the onset of shear thickening occurs at $\dot{\gamma}/\dot{\gamma}^\star = \mathcal{O}(1)$. In the supplementary material, we further elaborate on this, examining the relationship between the critical shear rate $\dot{\gamma}^\star$ and the critical shear stress $\sigma^\star$.

C. Shear-thinning rheology

In repulsive-particle suspensions, in the Stokesian limit, the drag force must balance the lubrication force and the repulsive force [given by Eq. (35)]; thus, we have

$$6\pi\eta_e a(\dot{\gamma}a - v)\varepsilon^{-3.70}$$
$$\sim (3/2)\pi a^2 \eta_e(v/h) + F_0 e^{-(h-\delta)\kappa}. \tag{53}$$

Setting $v = 0$, we obtain

$$6\pi\eta_e a^2 \dot{\gamma}\varepsilon^{-3.70} \sim F_0 e^{-(H-\delta)\kappa}, \tag{54}$$

and hence,

$$(H - \delta)\kappa \sim \ln\left(\frac{\dot{\gamma}^\star}{\dot{\gamma}}\right), \tag{55}$$

where H is the distance between particle surfaces at which the repulsive force balances the largest value of the drag force. In these conditions, the suspension behaves as if it were formed by larger frictionless particles, referred to in the following as *apparent particles*, with a radius equal to that of the actual particles (hard core) plus the thickness of a *soft shell* of liquid equal to half the equilibrium distance H. In other words, for $\dot{\gamma}/\dot{\gamma}^\star \leq 1$, particle 2 stops at a distance H (from particle 1) greater than δ, so the system behaves as a

suspension of larger noncontacting particles with radius $r \equiv a + H/2$. The corresponding jamming volume fraction of the actual particles, denoted as $\phi_j^\star$, is equal to

$$\phi_j^\star = \phi_j\left(\frac{r}{a}\right)^{-3} = \phi_j\left[1 + \frac{H}{2a}\right]^{-3}, \tag{56}$$

where ϕ_j is the jamming volume fraction of the apparent (frictionless) particles. Then, the suspension viscosity is given by

$$\eta_r = C\left[1 - \left(\phi/\phi_j^\star\right)\right]^{-\lambda}. \tag{57}$$

As $\dot{\gamma}/\dot{\gamma}^\star$ increases, H reduces [Eq. (55)], $\phi_j^\star$ increases [Eq. (56)], and so the suspension viscosity decreases [Eq. (57)]. The shear-thinning behavior is expected to cease when $\dot{\gamma}/\dot{\gamma}^\star$ reaches unit order of magnitude, an expectation corroborated by numerical simulations (including ours) and experimental data. For more details, we refer to the supplementary material.

Note that the suspension does not strictly jam at $\phi_j^\star$; rather, it develops a yield stress with magnitude set by the interparticle repulsive strength. $\phi_j^\star$ represents the extrapolated volume fraction at which the viscosity diverges under a given imposed shear rate or stress. At volume fractions slightly above $\phi_j^\star$, the suspension does not flow under that same imposed shear rate or stress, but flow may be recovered—i.e., the suspension may *yield*—if the stress is increased.

D. On the suspension of apparent particles

As described, in the shear-thinning region, the suspension can be regarded as formed of larger, frictionless, soft particles, with a radius $a + H/2$. Each apparent particle consists of a rigid core, represented by a real particle, and a liquid shell of thickness $H/2$, with H given by Eq. (55). The relative viscosity of this suspension is given by Eq. (57), where ϕ and $\phi_j^\star$ denote the volume fraction and the jamming volume fraction of the real particles, respectively. This equation can also be written in terms of the volume fraction $\phi_a = \phi(r/a)^3$ and jamming volume fraction ϕ_j of the apparent particles as follows:

$$\eta_r = C\left[1 - (\phi_a/\phi_j)\right]^{-\lambda}. \tag{58}$$

In this equation, ϕ_j is a constant, while ϕ_a is a function of the shear rate (since it depends on r and thus on H).

Having *soft interpenetrable shells*, the apparent particles are not equivalent to frictionless rigid particles and should not be expected to behave exactly like them. As discussed in more detail below, we assume that the jamming volume fraction of the apparent particles is equal to that of frictionless rigid particles, but we allow the exponent λ to be lower, to reflect the lower viscosity that a suspension of frictionless soft particles has compared to a suspension of frictionless rigid particles. This is supported by results available in the literature [29,30].

VI. RESULTS AND DISCUSSION

We begin by examining suspensions of nonrepulsive particles, identifying the conditions under which, in simple shear flow, the fluid velocity profile departs from linearity, making it necessary to resolve the dynamics of the fluid phase. Next, we present the relative viscosity as a function of the solid volume fraction for suspensions of nonrepulsive frictionless and frictional particles; these curves yield the corresponding values of the jamming volume fraction, which are subsequently used in the discussion of the rheology of suspensions of repulsive frictional particles. Finally, we consider suspensions of repulsive frictional particles, first investigating the rheology of a system with $\phi = 0.55$ and $\kappa^{-1} = 0.05a$ and then exploring the influence of the Debye length by extending the analysis to systems with $\kappa^{-1} = 0.025a$, $0.005a$, and $0.0005a$.

Our analysis builds on Sec. V, focusing on the jamming volume fraction $\phi_j^{\star}$ and on the exponent λ as functions of the dimensionless shear rate $\dot{\gamma}/\dot{\gamma}^{\star}$.

A. Nonrepulsive particle suspensions

A key feature of our CFD-DEM model is that the velocity fields—in particular that of the fluid phase—are not prescribed but calculated, emerging from the velocity difference imposed by the boundary walls (refer to Fig. 1). In an ideal simple shear flow, in which the fluid and solid phases have the same mean velocity, and the properties of the suspension are uniform, the shear rate has the same value in the entire flow domain; thus, calculating the fluid velocity field is unnecessary. However, at large solid volume fractions, local and intermittent jamming produces interphase slip and deviations from linearity. While such deviations may vanish when averaged over time, they can nevertheless give rise to a complex rheological response close to the jamming transition.

1. Velocity profiles at low and high solid volume fraction

Figure 2 shows the instantaneous profiles of the x component of the fluid- and solid-phase velocities and of the shear
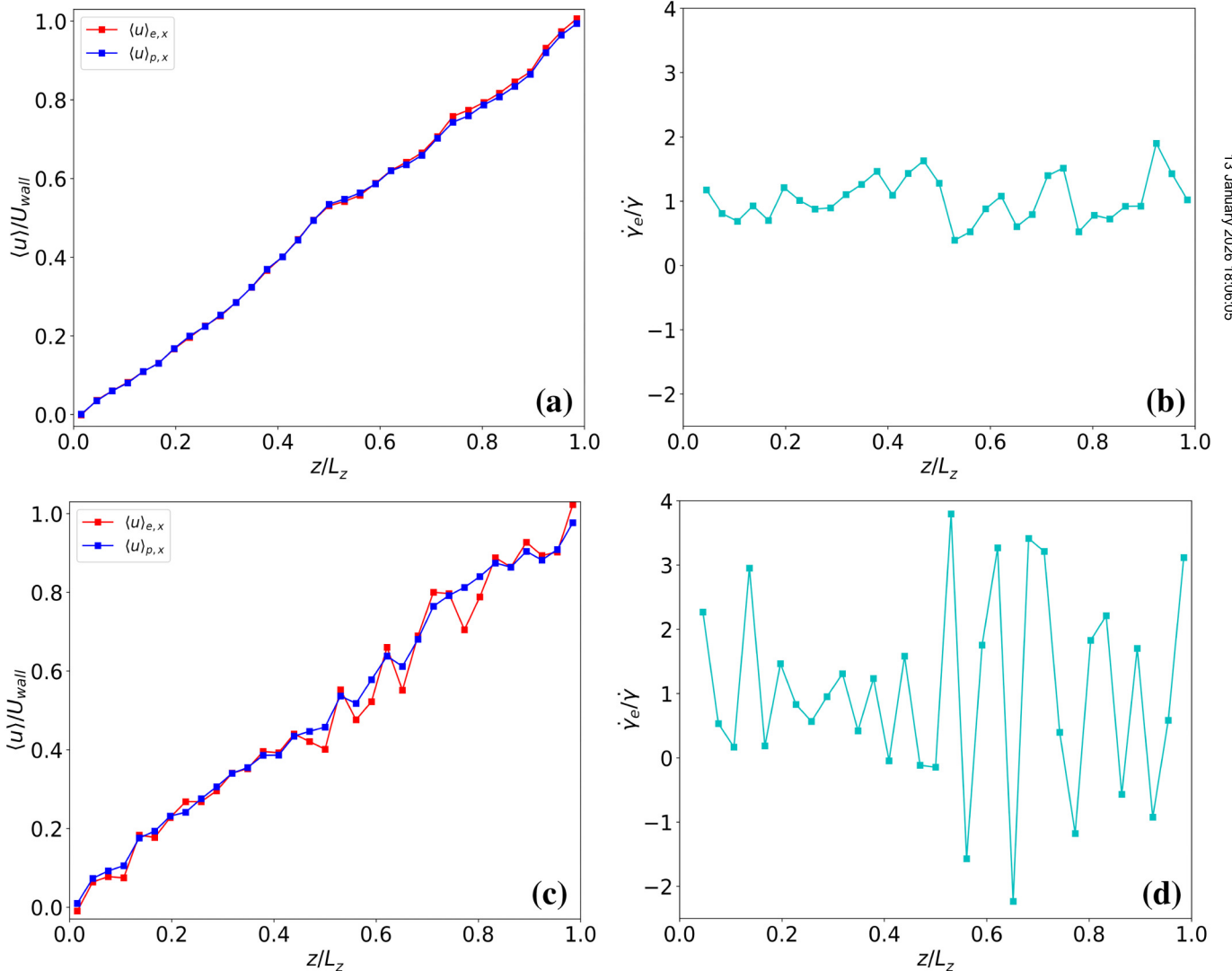

FIG. 2. (a) and (b) Instantaneous profiles of the normalized fluid and solid velocities and of the normalized fluid shear rate for a suspension with an overall solid volume fraction of 0.48. (c) and (d) Analogous results for a suspension with an overall solid volume fraction of 0.58. The profiles are taken at a time approximately equal to 300 units of strain.

rate of the fluid phase (i.e., $\langle u \rangle_{e,x}$, $\langle u \rangle_{p,x}$, and $\dot{\gamma}_e$) for two suspensions of nonrepulsive frictional rigid particles with a nominal solid volume fraction of 0.48 and 0.58, and a jamming volume fraction of 0.61 (this value is obtained from Fig. 4. which we will discuss later). The profiles are sampled at a time $t \approx 300/\dot{\gamma}$. Figures 2(a) and 2(b), corresponding to the less dense suspension, confirm our expectation that, far from the jamming point, the ideal-behavior assumption holds: The interphase slip velocity is negligible, the velocity profiles are linear, and the shear rate is nearly uniform and equal to the nominal value of U_{wall}/L_z. Conversely, Figs. 2(c) and 2(d) indicate that, sufficiently close to jamming, the suspension no longer exhibits a linear velocity profile and a uniform shear rate across the entire flow domain. In localized regions, the interphase slip velocity fluctuates, the fluid velocity profile becomes nonlinear, and the shear rate deviates from its nominal value. These regions vary in time, but the instantaneous profiles are never ideal.

This departure from ideal flow intensifies as the suspension nears jamming. To understand its origin, it is, therefore, useful to analyze the system at the jamming point; this is convenient not only because there the deviation is maximal but also because, since at jamming the particles are immobile, the equations of motion for the fluid phase can be solved analytically to determine the velocity profile.

2. Fluid shear flow through motionless particles

Treating the jammed solid as a stationary porous medium, the momentum balance equation for the fluid can be solved (a detailed analysis is given in the supplementary material) to yield the following steady-state velocity profile,

$$\frac{\langle u \rangle_{e,x}}{U_{wall}} = \frac{\sinh(z/\xi)}{\sinh(L_z/\xi)}, \tag{59}$$

with

$$\xi \equiv \left[\frac{\eta_e}{\eta_{BG} - \phi\eta_e} \cdot \frac{9\phi(1-\phi)^{-3.7}}{2a^2} \right]^{-1/2}, \tag{60}$$

where η_{BG} is the Batchelor and Green (BG) viscosity [Eq. (42)]. We also solved the problem numerically, validating the results of the CFD-DEM model using Eq. (59).

Figure 3(a) reports $\langle u \rangle_{e,x}/U_{wall}$ versus the spatial coordinate z for a system of immobile particles with a solid volume fraction of 0.55. Both analytical and numerical profiles are shown. In the simulation, the particles were kept fixed, and the CFD cells had a $10\,\mu m$ side-length. The simulation results (red crosses) closely match the analytical solution (blue line), revealing a highly nonlinear velocity profile with a boundary layer forming near the moving wall, consistent with the results reported by Kuznetsov [54] for a shear flow through a stationary porous medium. For $\phi = 0.55$, the boundary layer width is $\approx 8\,\mu m$; therefore, with the CFD cells used, in this region the velocity profile cannot be fully resolved; nevertheless, the width of the boundary layer is predicted correctly. The velocity profile depends mainly on ϕ;
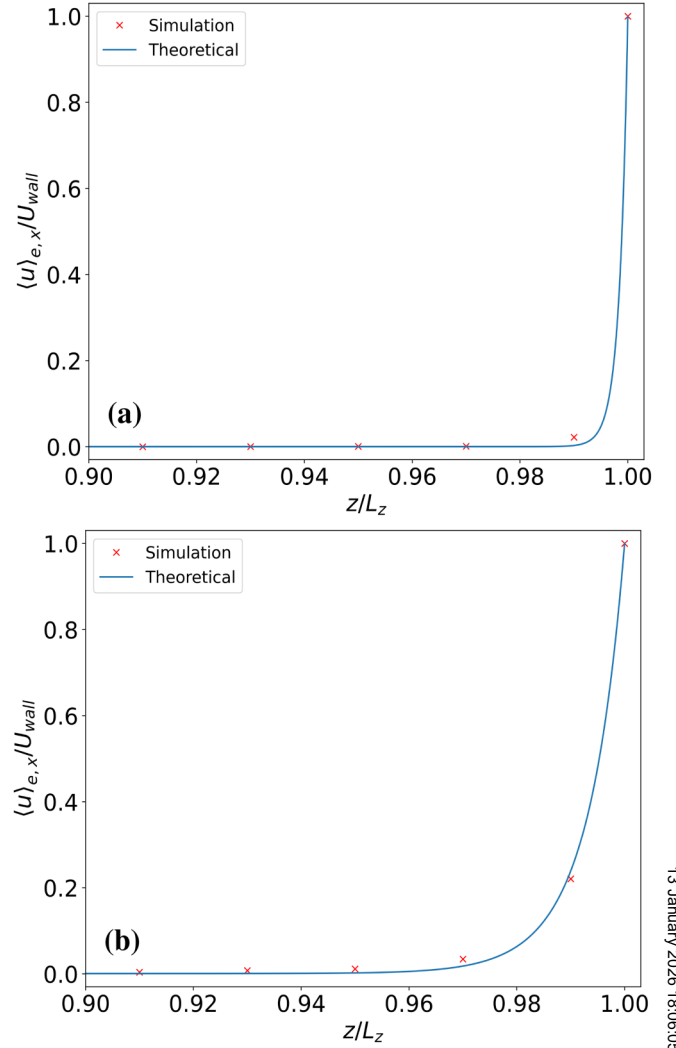

FIG. 3. (a) Magnified view of the normalized fluid velocity profile $\langle u \rangle_{e,x}/U_{wall}$ as a function of normalized height z/L_z, where L_z is the height of the flow domain in the z direction and U_{wall} is the velocity of the upper wall. The particles are immobile, and the nominal solid volume fraction is $\phi = 0.55$. (b) Analogous results for a suspension with a nominal $\phi = 0.10$. See supplementary material for a full view of the fluid velocity profile.

therefore, to better judge the precision of our model, we repeated the simulation for $\phi = 0.1$. As shown in Fig. 3(b), here the numerical model predicts well the boundary layer width of $\approx 30\,\mu m$.

These results indicate that, in dense suspensions, the fluid velocity profile is expected to be nonlinear in regions where the particle network is jammed, leading to a complex rheological response near the jamming point that is not fully captured by models in which a linear fluid velocity field is imposed. In addition, the close agreement between the simulation results and the analytical solution demonstrates the accuracy of our CFD-DEM model.

Having examined the flow of the fluid phase, we now turn to the viscosity of the suspension.

3. Viscosity divergence

Here, we determine the jamming volume fractions of nonrepulsive particles, anticipating that these dictate the limiting
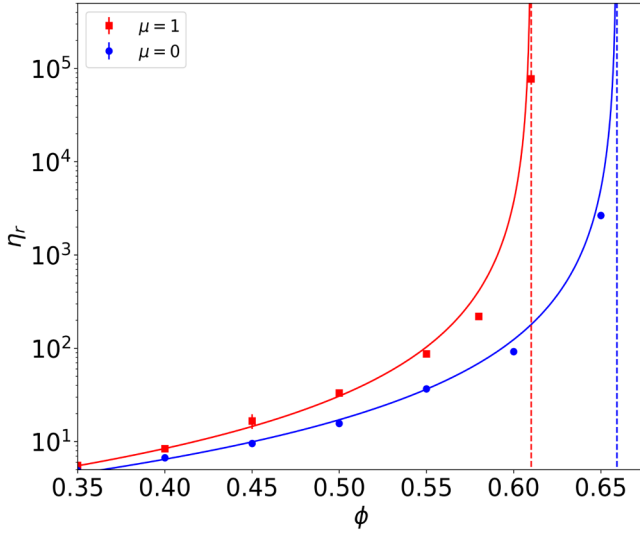
FIG. 4. Relative viscosity η_r as a function of the solid volume fraction ϕ for suspensions of frictionless ($\mu = 0$, blue dots) and frictional ($\mu = 1$, red squares) nonrepulsive particles. Here, η_r is independent of shear rate $\dot{\gamma}$ because the Stokes number and the ratio $6\pi\eta_e a\dot{\gamma}/k^n$ are significantly smaller than unity (see Sec. IV). By fitting to the KD equation [Eq. (51), red and blue lines], we obtain $\phi_j = 0.66$ for the frictionless particles and $\phi_j = 0.61$ for the frictional particles, with $C = 1$ and $\lambda = 2$. The dashed red and blue vertical lines mark the ϕ_j values of the frictional and frictionless particles, respectively. See supplementary material for a comparison with literature data.

rheology of the repulsive particle suspension for $\dot{\gamma}/\dot{\gamma}^{\star} \approx 1$ (frictionless particles) and $\dot{\gamma}/\dot{\gamma}^{\star} \gg 1$ (frictional particles). Figure 4 reports the relative viscosity η_r as a function of ϕ for nonrepulsive particles with friction coefficients of $\mu = 1$ and $\mu = 0$. Fitting the KD equation [Eq. (51)] to the data, we retrieve jamming volume fractions of $\phi_j = 0.61$ (frictional) and $\phi_j = 0.66$ (frictionless), having set $C = 1$ and $\lambda = 2$. This value of λ is consistent with experiments [55] and prior simulations [56], although different values have also been reported (see, for instance, Zarraga *et al.*, [57]). The obtained values of ϕ_j are marginally higher than those from other numerical models [6,58], likely due to the presence in our model, at large ϕ, of deviations from a linear velocity profile. However, the trend with respect to μ, important for the following discussion, is consistent. For a comparison between the rheological curves reported in Fig. 4 and experimental and numerical data from the literature, we refer to the supplementary material.

B. Repulsive particle suspensions

We now introduce the repulsive forces described by Eq. (35), considering a suspension with $\phi = 0.55$ and a Debye length $\kappa^{-1} = 0.05a$. The rate-dependent rheology shown in Fig. 5 serves as a reference for subsequent comparisons with results obtained at other values of κ^{-1}.

1. Viscosity contributions

Overall, the constitutive curve in Fig. 5 shows that the material shear-thins at low $\dot{\gamma}/\dot{\gamma}^{\star}$, shear-thickens at intermediate $\dot{\gamma}/\dot{\gamma}^{\star}$, and has constant viscosity at large $\dot{\gamma}/\dot{\gamma}^{\star}$. The horizontal dashed-dotted lines indicate the reported η_r in Fig. 4
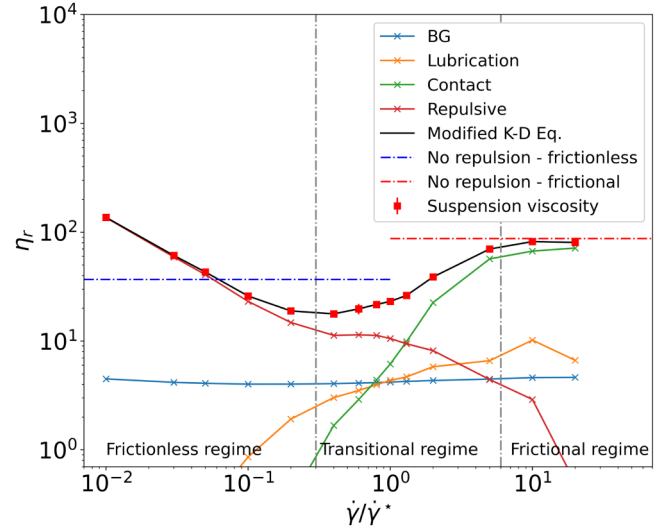

FIG. 5. Relative viscosity η_r as a function of dimensionless shear rate $\dot{\gamma}/\dot{\gamma}^{\star}$ (red squares) for a suspension of repulsive particles with $\kappa^{-1} = 0.05a$ and $\phi = 0.55$. The various contributions to the suspension viscosity are reported according to the legend. The horizontal dotted lines indicate the relative viscosity for suspensions of frictional (blue lower line) and frictionless (red upper line) particles in the absence of repulsive forces. The black line represents the modified KD equation [Eq. (57)], where $\phi^{\star}$ and λ are given by Figs. 7(a) and 7(b).

at $\phi = 0.55$ for nonrepulsive particles. The total relative viscosity (red squares) comprises contributions, as plotted in Fig. 5, from particle contacts, lubrication forces, repulsive forces, and the BG term. The latter is not shear-rate dependent and is close to its theoretical value of 4.7 predicted by Eq. (42). The lubrication contribution is significant but never dominates. The dominant viscosity contribution depends on $\dot{\gamma}/\dot{\gamma}^{\star}$, originating from either repulsive or contact interactions. The former dominates at $\dot{\gamma}/\dot{\gamma}^{\star} < 1$, where particles are hindered from coming into contact by electrostatic forces; the latter dominate at $\dot{\gamma}/\dot{\gamma}^{\star} > 1$, where repulsive forces are insignificant and the contact viscosity grows until reaching that of the corresponding suspension of nonrepulsive, frictional particles. The crossover value of $\dot{\gamma}/\dot{\gamma}^{\star} = 1$ indicates that the proposed nondimensionalization of the shear rate [Eq. (52)] is correct; this marks the point where the equilibrium distance between particles vanishes and direct contacts become widespread. Hence, we define three regimes, delineated in Fig. 5 by vertical dotted lines: a frictionless, shear-thinning regime at small $\dot{\gamma}/\dot{\gamma}^{\star}$; a transitional, shear-thickening regime at intermediate $\dot{\gamma}/\dot{\gamma}^{\star}$; and a frictional, rate-independent regime at large $\dot{\gamma}/\dot{\gamma}^{\star}$.

2. Pairwise separation H between particles

Before discussing our results in the context of the modified KD equation [Eq. (57)], we first test our estimate of the particle-particle equilibrium separation distance H [Eq. (55)]. To do so, we determine the effective added particle radius by analyzing a histogram of the force-weighted distribution of surface-to-surface distances between particles interacting via repulsive forces. Since larger forces contribute more to the viscosity, to which the value of H is ultimately related via Eqs. (56) and (57), we quantify this effect using the

following quantity:

$$\overline{h} \equiv \frac{\sum h_{rs}|\boldsymbol{f}_{rs}^i|}{\sum |\boldsymbol{f}_{rs}^i|}, \tag{61}$$

where h_{rs} is the surface-to-surface distance between particles r and s and $\boldsymbol{f}_{rs}^i$ is the repulsive force acting between them, given by Eq. (35).

Figure 6(a) shows the measured distributions of particle separations h scaled by our estimate H, for the suspension within the transitional regime at $\dot{\gamma}/\dot{\gamma}^\star = 0.4$. The weighted mean distance $\overline{h}/H$ is marked by a red vertical line. Although the distribution in Fig. 6(a) is broad, and a considerable number of direct particle contacts occur [at $h = \delta$, the distribution function $g(h)$ does not vanish], there is a good match between the theoretical equilibrium distance ($h/H = 1$), the weighted mean distance ($\overline{h}/H$), and the largest peak of the histogram.

In Fig. 6(b), we extend this analysis by reporting $\overline{h}$ and H as functions of $\dot{\gamma}/\dot{\gamma}^\star$. For $\dot{\gamma}/\dot{\gamma}^\star < 0.4$, the estimated equilibrium distance H slightly overestimates the weighted mean distance $\overline{h}$, the error being within 30%. Nonetheless, the two quantities have the same order of magnitude; thus, we conclude that the force balance in Eq. (54) holds, and Eq. (55) estimates H well. To make the predictions of Eq. (55) consistent with the values of $\overline{h}$ obtained numerically, we modify the equation as follows:

$$(H - \delta)\kappa = \alpha \ln\left(\frac{\dot{\gamma}^\star}{\dot{\gamma}}\right), \tag{62}$$

where on the right-hand side, we have introduced the parameter α (having unit order of magnitude) allowing us to represent the expression as an equality. For further details, see the supplementary material. In the following, to describe the shear thinning more accurately, we use the parameter α to fine-tune the equilibrium distances used for the viscosity predictions on the basis of the surface-to-surface distance distributions obtained from the simulations.

3. Measuring the KD parameters $\phi_j^\star$ and λ

After confirming that our estimate of H is correct within a factor of order one, we now examine the implications of this result for our viscosity predictions in the frictionless regime using the KD equation. To do so, we first set $\phi_j = 0.66$ in this region—the value obtained in Fig. 4 for frictionless rigid particles, representing the random close packed limit for bidisperse spheres. Similarly, in the frictional regime, we set $\phi_j = 0.61$, as measured in Fig. 4. Finally, in the transitional regime, we let ϕ_j vary in proportion to $\ln(\dot{\gamma}^\star/\dot{\gamma})$, interpolating between the frictionless and frictional values.

Having thus specified the rate dependence of ϕ_j, we next compute the rate dependence of $\phi_j^\star$ via Eq. (56), with H given by the weighted mean distance measured by simulation. The variation in both jamming volume fractions is reported in Fig. 7(a). In the shear-thinning region, as $\dot{\gamma}/\dot{\gamma}^\star$ increases, the thickness H of the fluid shells surrounding the particles decreases, $\phi_j^\star$ accordingly increases, and the suspension, at fixed ϕ, finds itself further away from the relevant jamming point, resulting in a viscosity reduction.

Interestingly, at the crossover between the frictionless and transitional regimes, the suspension of repulsive particles exhibits a lower viscosity than that of frictionless rigid particles. This cannot be explained only on the basis of a rate-dependent jamming point that takes rigid particle values as its upper limits. To capture this, we let the exponent λ be $\dot{\gamma}/\dot{\gamma}^\star$-dependent and calculate its value using the viscosities measured in Fig. 5 and the modified KD equation [Eq. (57)]. Setting $C = 1$ and taking $\phi_j^\star(\dot{\gamma}/\dot{\gamma}^\star)$ from Fig. 7(a), we obtain the profile shown in Fig. 7(b). The black line plotted in Fig. 5 represents the viscosity thus obtained with the modified KD equation.

4. Quantifying the apparent particle softness

To understand the rate-dependence of λ reported in Fig. 7(b), we quantify the softness of the apparent particles,
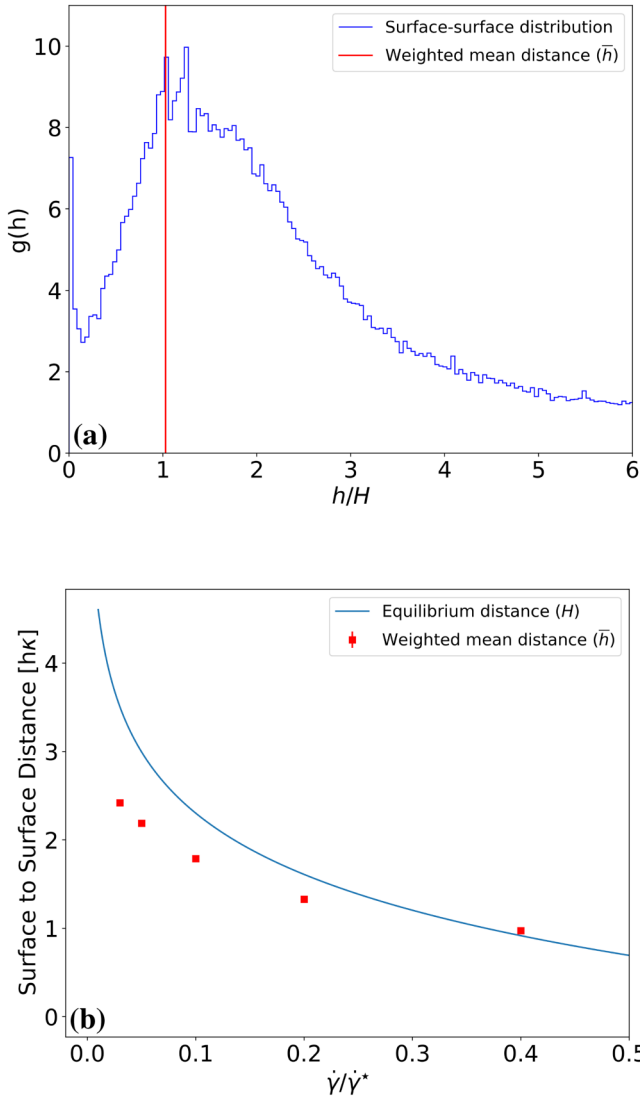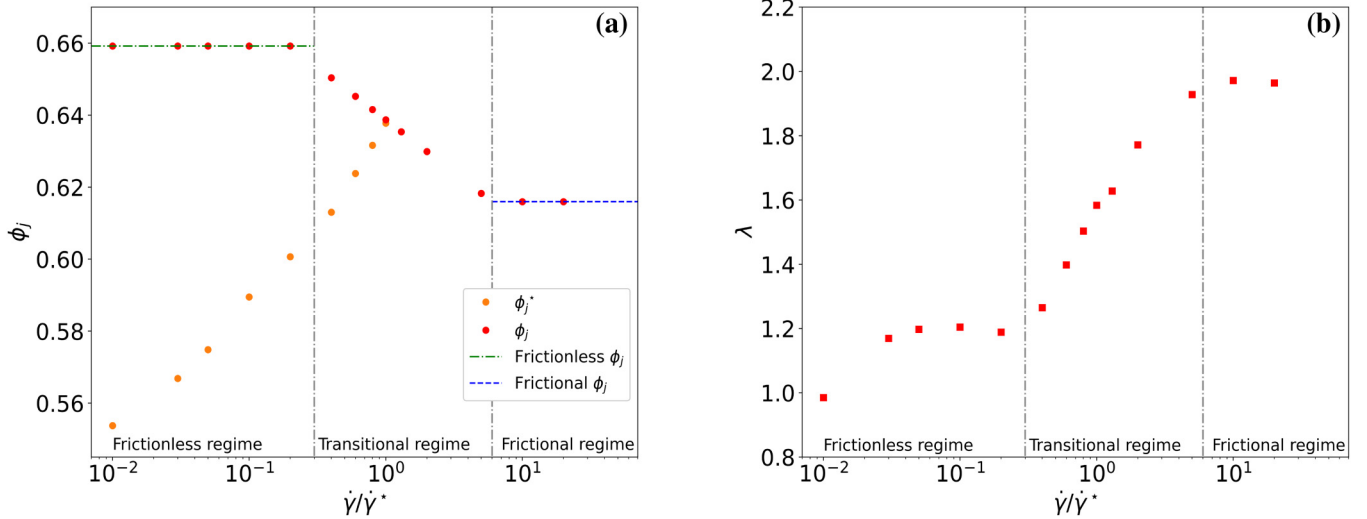
FIG. 6. (a) Radial distribution function for the suspension at $\dot{\gamma}/\dot{\gamma}^\star = 0.4$, $\phi = 0.55$, and $\kappa^{-1} = 0.05a$. The surface-to-surface distance (h) is normalized by the theoretical equilibrium distance H [Eq. (55)]. The normalized force-weighted mean distance ($\overline{h}/H$) calculated by Eq. (61) is marked by a vertical red line. (b) Weighted mean distance ($\overline{h}$) and theoretical equilibrium distance (H) normalized by the Debye length (κ^{-1}) for a suspension with $\phi = 0.55$, as a function of $\dot{\gamma}/\dot{\gamma}^\star$.

FIG. 7. (a) Jamming volume fractions as functions of $\dot{\gamma}/\dot{\gamma}^{\star}$. The values of ϕ_j in red upper circles are assumed to be constant at 0.66 in the frictionless regime (dotted-dashed green line). In the transitional regime, ϕ_j is assumed to decrease in proportion to $\ln(\dot{\gamma}^{\star}/\dot{\gamma})$ from the frictionless to the frictional values. In the frictional regime, $\phi_j = 0.61$ (dashed blue line). The values of $\phi_j^{\star}$ (orange lower circles) are calculated from Eq. (56) using the interparticle weighted mean distance ($\bar{h}$) shown in Fig. 6(b). (b) Exponent λ of the modified KD equation [Eq. (57) with $C = 1$ and $\phi_j^{\star}$ given in Fig. 7(a)] as a function of $\dot{\gamma}/\dot{\gamma}^{\star}$.

addressing the particle pair force balance in Eq. (54). As demonstrated in Fig. 6(a), our assumption that the apparent particles of radius $a + H/2$ do not overlap is not strictly correct. Small overlaps are present and imply that the particle pairs are not in mechanical equilibrium and are, thus, subjected to repulsive forces. We model these here as linearly elastic, allowing us to quantify an effective spring coefficient. To estimate it, we assume that the distance h between the surfaces of two real particles is slightly smaller than H, so the net force between the particles is a repulsive force equal to

$$F_R = F_0 e^{-(h-\delta)\kappa} - F_d. \tag{63}$$

where $F_d = 6\pi\eta_e a^2 \dot{\gamma}\varepsilon^{-3.70}$. Since h is slightly smaller than H, we can expand F_R around H and retain only the linear part of the expansion. This yields

$$F_R \sim F_0 e^{-(H-\delta)\kappa} - \kappa F_0 e^{-(H-\delta)\kappa}(h - H) - F_d. \tag{64}$$

Defining $\zeta \equiv H - h$ as the overlap between apparent particles and using Eq. (54), we can express Eq. (64) as follows:

$$F_R \sim \left[\kappa F_0 e^{-(H-\delta)\kappa}\right]\zeta = (\kappa F_d)\zeta. \tag{65}$$

Thus, because by approximation F_R is linear in the overlap ζ, we can regard it as an elastic force, whose elastic constant (or spring coefficient) is

$$k_R \sim \kappa F_d. \tag{66}$$

For a Debye length of $0.05a$, and with the parameter values reported in Table I, the apparent spring coefficient is four orders of magnitude smaller than the spring coefficient k^n of real rigid particles.

This softness likely explains the important observation in the above rheology that the viscosity at the crossover between the frictionless and transitional regimes drops below that measured for frictionless rigid spheres. This is captured by our modified KD equation, in which variation in λ permits rate dependence in η_r even when ϕ_j is fixed at its upper value. Generally, for a given pairwise force magnitude, softer particles can sustain larger overlaps than harder particles. This means that under a given shear rate, the energy barrier required to transition between two microstructural states is, in relative terms, smaller for soft particles than for hard ones. Therefore, we expect that at volume fractions close to jamming, the hard particle suspension will arrange into structured force chains, whereas the soft particles will be able to move more freely past their neighbors, by overlapping, to reach states of fewer contacts and thus lower stress. Thus, we conclude that suspensions of repulsive particles are microstructurally distinct from suspensions of nonrepulsive rigid frictionless particles, even at modest $\dot{\gamma}/\dot{\gamma}^{\star}$ for which H is small, consistent with them having markedly different viscosities η_r and exponents λ.

C. Rheology of repulsive particle suspensions: Influence of the Debye length

In this section, we consider four repulsive suspensions with solid volume fraction $\phi = 0.55$ and Debye lengths of $0.0005a$, $0.005a$, $0.025a$, and $0.05a$. Figure 8 reports their relative viscosity against the dimensionless shear rate; the trends resemble that shown in Fig. 5. As before, all the suspensions are frictionless for $\dot{\gamma}/\dot{\gamma}^{\star} \lesssim 0.3$, where direct particle contacts are essentially absent. In this region, the suspensions shear-thin, and larger Debye lengths yield steeper shear-thinning profiles, for H decreases more rapidly with increasing $\dot{\gamma}/\dot{\gamma}^{\star}$ [Eq. (55)]. As the Debye length reduces, the viscosity in the frictionless regime loses its rate dependence, its value converging toward that reported in Fig. 4 for the nonrepulsive
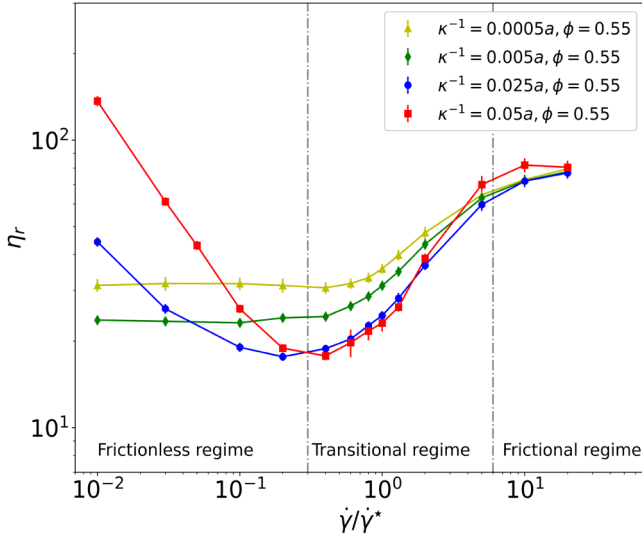
FIG. 8. Relative viscosity η_r as a function of $\dot{\gamma}/\dot{\gamma}^{\star}$ for suspensions with $\phi = 0.55$ and $\kappa^{-1} = 0.0005a, 0.005a, 0.025a,$ and $0.05a$ in yellow triangles, green diamonds, blue circles, and red squares, respectively. The lines represent the modified KD equation [Eq. (57)] where $\phi_j^{\star}$ and λ are given by Figs. 9(a) and 9(b), respectively.

frictionless suspension. In the region where $\dot{\gamma}/\dot{\gamma}^{\star} \sim 1$, the number of particles in direct contact gradually increases with $\dot{\gamma}/\dot{\gamma}^{\star}$, so the suspensions shear-thicken. As the particle-contact viscosity becomes dominant, the viscosity profiles converge, eventually collapsing in the frictional regime into one profile, that of the suspension of nonrepulsive frictional rigid particles.

The corresponding profiles of the jamming volume fraction $\phi_j^{\star}$ and of the KD exponent λ are reported in Fig. 9 and show a similar trend: In the frictionless regime, they strongly depend on the Debye length, while in the transitional regime they converge, eventually collapsing in the frictional regime with plateau values of $\phi_j^{\star} = 0.61$ and $\lambda = 2$, consistent with the suspension of nonrepulsive frictional particles.

In the frictionless regime, $\phi_j^{\star}$ increases with $\dot{\gamma}/\dot{\gamma}^{\star}$, its profile becoming steeper as the Debye length increases, in line with Eqs. (55) and (56). Conversely, λ depends weakly on $\dot{\gamma}/\dot{\gamma}^{\star}$ but decreases significantly as the Debye length increases. This decrease reflects the lower viscosity that suspensions of softer particles have compared to suspensions of harder particles. Softer particles can deform more easily than harder particles, meaning that under a given shear rate, the energy barrier required to transition between two microstructural states is, in relative terms, smaller for softer particles than for harder ones. Consequently, softer particles are able to move more freely past their neighbors and reach states of fewer contacts and thus lower stress. For the apparent particles considered in this work, this effect is enhanced when the thickness of the liquid shells surrounding the rigid particles increases. Now, when the Debye length increases, both the softness of the apparent particles and the thickness of the liquid shells increase [Eqs. (55) and (66)], and this results in a significant reduction in the exponent λ. Varying the shear rate affects λ less significantly, because while reducing $\dot{\gamma}/\dot{\gamma}^{\star}$ or increasing κ^{-1} affects the apparent particle softness equally [Eq. (66)], the effect on the thickness of the liquid shells is markedly different [Eq. (55)]. For instance, increasing κ^{-1} or reducing $\dot{\gamma}$ by two orders of magnitude affects the liquid shell thickness quite differently: In the first case, the thickness increases 100 times, while in the second case it merely doubles. This suggests that the Debye length should affect λ much more than the shear rate, in line with what the simulations show.

One last consideration is in order. From this discussion, one might expect that in the frictionless regime, the viscosity of the repulsive suspension with the largest Debye length ($\kappa^{-1} = 0.05a$) should be the lowest (since λ is the lowest). This would be true if the jamming volume fraction $\phi_j^{\star}$ were the same for all the suspensions, but as we see in Fig. 9(a), this is not the case. The suspension with the largest Debye length has also the smallest jamming volume fraction;
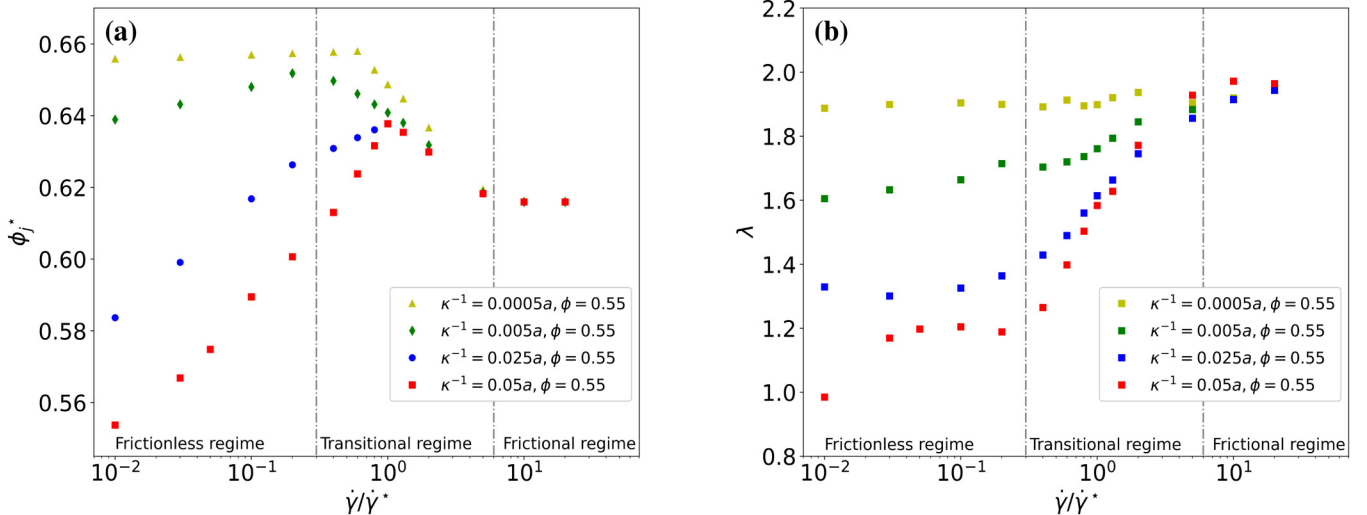

FIG. 9. (a) Jamming volume fraction $\phi_j^{\star}$ [Eq. (56)] calculated using the assumed ϕ_j and the weighted mean distance $\overline{h}$. In both figures, the frictionless, transitional, and frictional regimes are marked by vertical dotted gray lines. (b) λ as a function of $\dot{\gamma}/\dot{\gamma}^{\star}$ for suspensions with $\phi = 0.55$ and $\kappa^{-1} = 0.0005a, 0.005a, 0.025a,$ and $0.05a$ in yellow triangles, green diamonds, blue circles, and red squares, respectively.

moreover, both $\phi_j^\star$ and λ are functions of the shear rate; this complex interplay results in the viscosity curves reported in Fig. 8.

VII. CONCLUSIONS

We have developed a CFD-DEM model for simulating suspensions of neutrally buoyant, non-Brownian, repulsive particles dispersed in a Newtonian fluid, considering all the relevant fluid and interparticle interactions. The model allows to analyze the dynamics and rheology in suspensions with medium to large solid volume fractions and any short-ranged repulsive force. Since these systems are overdamped and the traditional Belytschko criterion is insufficient, we introduced a new time step criterion that accounts for lubrication forces.

A key feature of the model is that it resolves both the fluid and particle velocity fields, eliminating the need to prescribe the fluid velocity field, as instead is done in simpler models that assume ideal simple shear flow. This allows to investigate the flow behavior near the jamming transition, where the solid phase becomes immobile and the fluid develops a velocity boundary layer. We derived an analytical expression for the boundary layer velocity profile, which the simulations accurately reproduced. Close to jamming, local and intermittent jamming of the particle phase leads to complex flow profiles, yet the model still recovers the viscosity divergence predicted by the Krieger–Dougherty equation.

We then used the model to investigate the rheology of suspensions of repulsive particles, performing simulations at a solid volume fraction of 0.55 and Debye lengths ranging from $0.0005a$ to $0.05a$. Using a simple force balance and accounting for the hindrance function in the expression for the drag force, we proposed a new scale for the shear rate marking the onset of shear thickening ($\dot{\gamma}^\star$) and obtained an expression for the interparticle equilibrium distance (H) as a function of this shear rate and the Debye length. The simulation results confirmed these predictions: Shear thickening occurred when $\dot{\gamma}/\dot{\gamma}^\star \sim 1$, and H was correctly estimated across all the shear rates and Debye lengths considered.

Treating repulsive particles as apparent particles consisting of a rigid core surrounded by a soft shell of thickness $H/2$, we described the suspension rheology using a modified Krieger–Dougherty equation. This revealed three regimes: a frictionless regime, characterized by shear thinning and no direct particle contacts; a transitional regime, characterized by shear thickening and a gradually increasing number of direct particle contacts; and a frictional regime, characterized by a constant viscosity, where direct particle contacts dominate. Assuming that the jamming volume fraction of the apparent particles (ϕ_j) is equal to that of frictionless rigid particles in the frictionless regime, is a decreasing function of the shear rate in the transitional regime, and is equal to that of frictional rigid particles in the frictional regime, we observed that the apparent particles exhibit an exponent λ smaller than that of rigid particles and decreasing with increasing Debye length.

To explain the value and shear-rate dependence of λ, we derived an expression for the elastic constant of the apparent particles. Since this is considerably smaller than that of rigid particles, apparent particles can be regarded as soft. This leads to a relatively smaller resistance to the flow of the suspension and to an increased ability of the particle network to deform, generating a lower viscosity compared to the rigid particles. Since the elastic constant of the apparent particles is inversely proportional to the Debye length, larger Debye lengths yield softer apparent particles, resulting in lower values of λ.

SUPPLEMENTARY MATERIAL

The supplementary material is organized into six sections. Section I summarizes the balance equations of the CFD-DEM model with all the required closures, reported in the final form implemented in the numerical code. Section II examines the critical shear rate ($\dot{\gamma}^\star$) that marks the onset of shear thickening, clarifying its physical meaning and its relationship with the more commonly used critical shear stress. A validation of our criterion for the onset of shear thickening is provided using experimental viscosity data from the literature. Section III discusses the advantages of modeling the dynamics of the fluid phase. For simple shear flow, we identify when and how the predictions of our model differ from those of models that assume a linear fluid velocity field. This section also includes a validation of our model's predictions for a set of simple flow problems. Section IV evaluates the accuracy of our viscosity predictions, comparing them with experimental and numerical data from the literature, first for suspensions of nonrepulsive particles and then for suspensions of repulsive particles. Section V presents representative spatial profiles (averaged in the flow and neutral directions) of the suspension velocity, shear rate, solid volume fraction, and relative viscosity. Finally, Section VI assesses the accuracy of the interparticle equilibrium distance estimated via the minimal physical model, showing that the parameter α, obtained from numerical simulations as a function of shear rate and Debye length, has unit order of magnitude across all cases considered in our work.

ACKNOWLEDGMENTS

AUTHOR DECLARATIONS
Conflict of Interest

The authors have no conflicts to disclose.

DATA AVAILABILITY

The data that support the findings of this study are available from the corresponding author upon reasonable request.

APPENDIX A: TIME STEP

A widely adopted criterion for selecting DEM time steps, called the Belytschko criterion, is given by $\Delta t_c = \sqrt{m/k^n}$ [59]. This criterion is commonly used for granular systems. But its validity for overdamped systems, such as particles immersed in a fluid, is questionable because overdamped

systems lack a natural angular frequency—the presence of this frequency being a key assumption in the Belytschko method. Therefore, for overdamped systems, we employ the amplification matrix method [60]. We start by deriving the Belytschko criterion to show what conditions must be satisfied for it to apply, then we derive a new time step criterion, and finally we compare the two criteria to highlight for what spring coefficient values our time step criterion must be used.

1. Absence of fluid-particle interactions

The equation of motion in the normal direction for a sphere involved in a linear viscoelastic collision with another identical particle reads

$$m\ddot{x} = -\eta^n \dot{x} - k^n x, \tag{A1}$$

where x is the position of the particle relative to the other particle, η^n is the normal damping coefficient, and k^n is the normal spring coefficient. Equation (A1) is the equation of a damped harmonic oscillator; rearranging it in terms of its frequency and damping coefficient yields

$$\ddot{x} + 2\psi\dot{x} + \kappa_0^2 x = 0, \tag{A2}$$

with

$$\psi \equiv \frac{\eta^n}{2m}; \quad \kappa_0^2 \equiv \frac{k^n}{m}, \tag{A3}$$

where κ_0 is the frequency of the undamped harmonic oscillator and ψ is the reduced damping coefficient. Equation (A2) can be solved analytically with initial conditions $x(0) = 0$ and $\dot{x}(0) = v_0$, where v_0 is the normal relative particle impact velocity. The solution is

$$x(t) = \frac{v_0}{\omega} e^{-\psi t} \sin(\omega t), \tag{A4}$$

$$\dot{x}(t) = \frac{v_0}{\omega} e^{-\psi t} [\omega\cos(\omega t) - \psi\sin(\omega t)], \tag{A5}$$

with $\omega \equiv \sqrt{\kappa_0^2 - \psi^2}$ denoting the natural angular frequency. For an explicit finite element method analysis, Belytschko expressed the critical time step as [60]

$$\Delta t_c = \frac{2}{\omega}. \tag{A6}$$

Expressing this equation in terms of the parameters featuring in Eq. (A1) yields

$$\Delta t_c = \frac{2}{\sqrt{\frac{k^n}{m} - \left(\frac{\eta^n}{2m}\right)^2}}. \tag{A7}$$

The time criterion of Eq. (A7) is smallest when $\eta^n = 0$ and can, thus, be represented by

$$\Delta t_c = \sqrt{\frac{m}{k^n}}, \tag{A8}$$

which retrieves the time step criterion presented in the Introduction. If the system is overdamped (that is, if $\kappa_0^2 < \psi$), Eq. (A7) does not have a real solution and cannot be used.

2. Presence of fluid-particle interactions

For particles immersed in a liquid, we must modify Eq. (A1) to consider the lubrication and drag forces. At contact, it is customary to fix the interparticle distance of the lubrication force to the surface roughness; thus, we write

$$m\ddot{x} = -\left[\eta^n + 6\pi\eta_e a\varepsilon^{-3.70} + (3/2)\pi a^2\eta_e/\delta\right]\dot{x} - k^n x + 6\pi\eta_e a^2\dot{\gamma}\varepsilon^{-3.70}, \tag{A9}$$

where η_e, a, and ε are the fluid viscosity, particle radius, and fluid volume fraction, respectively. Given a surface roughness of $\delta \sim 0.001a$, the lubrication force is the leading term of damping in Eq. (A9). By repeating the steps in Sec. A 1, we obtain the natural angular frequency,

$$\omega = \sqrt{\frac{k^n}{m} - \left[\frac{(3/2)\pi a^2\eta_e/\delta}{m}\right]^2}. \tag{A10}$$

For Eq. (A10) to have a real solution, k^n must be larger than ~ 2000 N/m, for $a = 5\,\mu$m, $\eta_e = 0.001$ Pa s, and $\rho = 1000$ kg/m^3, so that the system is underdamped. This value of k^n is larger than what is sometimes used in the literature [52]. Hence, we proceed to derive a time step criterion that does not require the system to be underdamped.

3. Amplification matrix method

The most common integrator scheme used by DEM software is the velocity Verlet integrator (used by LIGGGHTS and LAMMPS). The default velocity Verlet algorithm as used by LAMMPS and LIGGGHTS is the following:

1. $\dot{\mathbf{x}}_{n+(1/2)} = \dot{\mathbf{x}}_n + (\Delta t/2)\ddot{\mathbf{x}}_n,$
2. $\mathbf{x}_{n+1} = \mathbf{x}_n + \Delta t\dot{\mathbf{x}}_{n+(1/2)},$
3. $\ddot{\mathbf{x}}_{n+1} = \mathbf{F}/m = C\dot{\mathbf{x}}_{n+(1/2)} + k\mathbf{x}_{n+1} + \mathbf{f}/m,$
4. $\dot{\mathbf{x}}_{n+1} = \dot{\mathbf{x}}_{n+(1/2)} + (\Delta t/2)\ddot{\mathbf{x}}_{n+1},$

with

$$C \equiv -\frac{(3/2)\pi a^2\eta_e/\delta}{m}; \quad k \equiv -\frac{k^n}{m}, \tag{A11}$$

where C is related to the lubrication force [see the first term on the right-hand side of Eq. (A9), where, as done previously, the first two terms in square brackets have been neglected], k is related to the contact force [the second term on the right-hand side of Eq. (A9)], and $\mathbf{f}$ represents additional forces unrelated to the particle position and velocity [such as the last term on the right-hand side of Eq. (A9)]. Step 3 updates the acceleration considering the total force $\mathbf{F}$. Note that the forces are updated using the half time step velocity.

Let us rearrange the equations in steps 1 to 4 to express the updated variables in terms of the variables of the previous time step and simplify to one dimension,

$$\mathbf{d} = \mathbf{A}\mathbf{b} + \mathbf{c}, \qquad (A12)$$

with

$$\mathbf{A} \equiv \begin{bmatrix} 0 & 0 & \frac{\Delta t}{2} & 1 \\ 0 & 1 & \frac{\Delta t^2}{2} & \Delta t \\ 0 & k & \frac{k\Delta t^2}{2} + \frac{C\Delta t}{2} & k\Delta t + C \\ 0 & \frac{k\Delta t}{2} & \frac{\Delta t}{2}\left(1 + C\frac{\Delta t}{2} + \frac{k\Delta t^2}{2}\right) & 1 + \frac{\Delta t}{2}(C + k\Delta t) \end{bmatrix},$$

$$\qquad (A13)$$

$$\mathbf{b} \equiv \begin{bmatrix} 0 \\ x_n \\ \ddot{x}_n \\ \dot{x}_n \end{bmatrix}; \quad \mathbf{c} \equiv \begin{bmatrix} 0 \\ 0 \\ f/m \\ 0 \end{bmatrix}; \quad \mathbf{d} \equiv \begin{bmatrix} \dot{x}_{n+(1/2)} \\ x_{n+1} \\ \ddot{x}_{n+1} \\ \dot{x}_{n+1} \end{bmatrix}.$$

$\mathbf{A}$ is referred to as amplification matrix. For stability, its maximum absolute eigenvalue must be less than unity; this gives a condition for the maximum stable time step.

Calculating the eigenvalues of the amplification matrix is complex, so we have used PYTHON and the library "SymPy." The eigenvalues are as follows:

$$\lambda_1 = \frac{C\Delta t + \Delta t^2 k}{2} + \frac{\Delta t}{2}\sqrt{C^2 + 2C\Delta t k + \Delta t^2 k^2 + 4k} + 1,$$

$$\qquad (A14)$$

$$\lambda_2 = \frac{C\Delta t + \Delta t^2 k}{2} - \frac{\Delta t}{2}\sqrt{C^2 + 2C\Delta t k + \Delta t^2 k^2 + 4k} + 1,$$

$$\qquad (A15)$$

$$\lambda_3 = 0; \quad \lambda_4 = 0. \qquad (A16)$$

Using SymPy, we take the absolute values of λ_1 and λ_2, set them equal to unity, and solve for Δt. For both eigenvalues, we obtain the following critical time step:

$$\Delta t_c = \frac{-C \pm \sqrt{C^2 - 4k}}{k}. \qquad (A17)$$

In Eq. (A17), the negative sign (for the square root term) yields the only positive time step. This critical value is equivalent to that derived for the Euler integrator [60]. In an undamped system ($C = 0$), we roughly retrieve Belytschko's time criterion,

$$\Delta t_c = \sqrt{\frac{2m}{k^n}}. \qquad (A18)$$

Let us express Eq. (A17) in terms of the lubrication force and spring stiffness,

$$\Delta t_c = \frac{\sqrt{\left[(3/2)\pi a^2 \eta_e / \delta\right]^2 + 4mk^n}}{k^n} - \frac{(3/2)\pi a^2 \eta_e / \delta}{k^n}. \quad (A19)$$
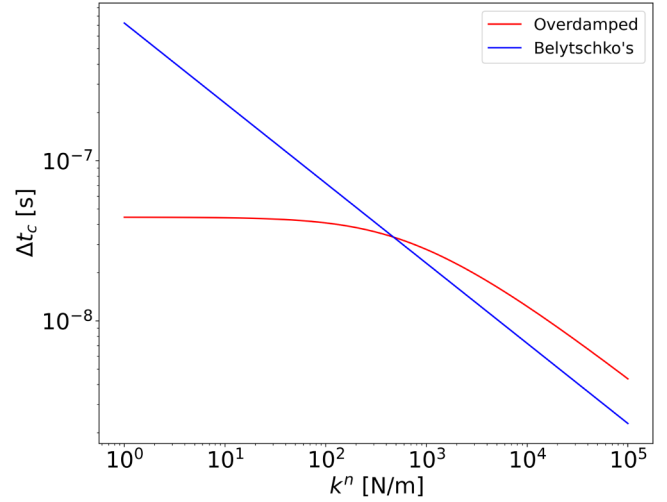

FIG. 10. Belytschko's time step criterion (blue straight line); new time step criterion for overdamped systems (red curved line). $a = 5\,\mu\text{m}$, $\delta = 0.001a$, $\eta_e = 0.001\,\text{Pa s}$, and $\rho = 1000\,\text{kg/m}^3$.

In Fig. 10, we compare the Belytscko time step criterion [Eq. (A8)] with our (overdamped) time step criterion [Eq. (A19)] as a function of the normal spring coefficient (k^n). From Fig. 10, we note that the Belytschko criterion highly overestimates the critical time step for small spring coefficients. The graph indicates that a spring coefficient less than $\sim 10^2$ N/m is unnecessary, since it does not result into a larger value of the critical time step. It is generally good to have a large spring coefficient to avoid largely overlapping particles, but this requires a smaller time step.

APPENDIX B: SHEAR RATE SCALE

Over the past decade, the prevailing notion has been that the onset of shear thickening, or the transition from frictionless to frictional rheology, is characterized by a dimensionless shear stress with a weak dependence on ϕ, while the corresponding dimensionless shear rate changes with ϕ more strongly [61]. Consequently, it has been common to discuss the onset of shear thickening in terms of shear stress, using the shear stress scale. But as we can see in Fig. 1(a) in the supplementary material, the dimensionless shear rate marking the transition from frictionless to frictional rheology is largely independent of ϕ. The marked dependence on ϕ reported in the literature stems from the classical definition of the drag force scale, taken to be equal to $6\pi\eta_e a^2 \dot{\gamma}$. This scale is accurate only for very dilute suspensions. To estimate the shear rate scale, we must prove Eq. (53) because from this equation the definition of $\dot{\gamma}^\star$ follows. Let us start from the general linear momentum balance equation for particle r interacting with particle s,

$$m\dot{\boldsymbol{u}}_r = \boldsymbol{f}_{d,r} + \boldsymbol{f}_{b,r} + \boldsymbol{f}_{rs}^\bullet + \boldsymbol{f}_{rs}^c + \boldsymbol{f}_{rs}^i + m\boldsymbol{g}, \qquad (B1)$$

where $\boldsymbol{f}_{b,r}$ is the buoyancy force. We assume a low Reynolds number and neutrally buoyant particles; then, the Stokes and Reynolds numbers are equal, and the inertia of the particles is negligible. For simplicity, here we define the buoyancy

force according to the Archimedes principle (this is convenient, because, for neutrally buoyant particles, the buoyancy force, and the weight force balance each other). As this definition differs from that employed in the main article, we must modify the closure for the drag force, to ensure that the total fluid-particle interaction force is modeled correctly [62]. The drag force based on the Archimedes definition of the buoyancy force, denoted as $f_{d,r}^A$, is related to the drag force adopted in the main article by the equation $f_{d,r}^A = f_{d,r}/\varepsilon$. As we consider particles r and s approaching, we can disregard the contact force f_{rs}^c. Thus, we can write

$$f_{d,r}^A + f_{rs}^\bullet + f_{rs}^i + V_p(\rho_p - \rho_e)g = 0, \qquad (B2)$$

where ρ_p is the density of particle r. Since we are considering neutrally buoyant particles, the last term in Eq. (B2) vanishes. Thus, Eq. (B2) reduces to

$$f_{d,r}^A = -f_{rs}^\bullet - f_{rs}^i. \qquad (B3)$$

In terms of orders of magnitude, we have

$$|f_{rs}^\bullet| \sim (3/2)\pi a^2 \eta_e(v/h); \quad |f_{rs}^i| \sim F_0 e^{-(h-\delta)\kappa}. \qquad (B4)$$

For the drag force, since we are considering a low Reynolds number, in Eq. (20), we set $\chi = 3.7$ and $C_D = 4.8^2/\text{Re}$. Thus, Eq. (18) yields

$$|f_{d,r}^A| \sim \frac{1}{\varepsilon}\left[(\pi a^2)\frac{1}{2}\left(\frac{4.8^2\eta_e}{2a\varepsilon}\right)\right]\varepsilon^{2-3.7}|\langle u\rangle_e - u_r|. \qquad (B5)$$

But it is

$$|\langle u\rangle_e - u_r| \sim \dot{\gamma}a - v. \qquad (B6)$$

Therefore, we obtain

$$|f_{d,r}^A| \sim 6\pi\eta_e a(\dot{\gamma}a - v)\varepsilon^{-3.70}. \qquad (B7)$$

Inserting Eqs. (B4) and (B7) into Eq. (B3), we obtain Eq. (53). This leads to Eq. (55), with $\dot{\gamma}^\star$ defined as per Eq. (52).

REFERENCES

[1] Jeffrey, D. J., and A. Acrivos, "The rheological properties of suspensions of rigid particles," AlChE J. **22**, 417–432 (1976).

[2] Zhu, Y., G. Lv, C. Song, B. Li, Y. Zhu, Y. Liu, W. Zhang, and Y. Wang, "Optimization of the washcoat slurry for hydrotalcite-based LNT catalyst," Catalysts **9**, 696 (2019).

[3] Jackson, R., "Locally averaged equations of motion for a mixture of identical spherical particles and a Newtonian fluid," Chem. Eng. Sci. **52**, 2457–2469 (1997).

[4] Blais, B., and F. Bertrand, "On the use of the method of manufactured solutions for the verification of CFD codes for the volume-averaged Navier–Stokes equations," Comput. Fluids **114**, 121–129 (2015).

[5] Manninen, M., and V. Taivassalo, *On the Mixture Model for Multiphase Flow* (Valtion Teknillinen Tutkimuskeskus, Espoo, Finland, 1996).

[6] Mari, R., R. Seto, J. F. Morris, and M. M. Denn, "Shear thickening, frictionless and frictional rheologies in non-Brownian suspensions," J. Rheol. **58**, 1693–1724 (2014).

[7] Cheal, O., and C. Ness, "Rheology of dense granular suspensions under extensional flow," Soc. Rheol. **62**, 501–512 (2018).

[8] Gillissen, J. J., and C. Ness, "Modeling the microstructure and stress in dense suspensions under inhomogeneous flow," Phys. Rev. Lett. **125**, 184503 (2020).

[9] Jamshidi, R., J. J. J. Gillissen, P. Angeli, and L. Mazzei, "Roles of solid effective stress and fluid-particle interaction force in modeling shear-induced particle migration in non-Brownian suspensions," Phys. Rev. Fluids **6**, 014301 (2021).

[10] Zhang, D., and A. Prosperetti, "Momentum and energy equations for disperse two-phase flows and their closure for dilute suspensions," Int. J. Multiphase Flow **23**, 425–453 (1997).

[11] Nott, P. R., E. Guazzelli, and O. Pouliquen, "The suspension balance model revisited," Phys. Fluids **23**, 043304 (2011).

[12] Ness, C., R. Seto, and R. Mari, "The physics of dense suspensions," Annu. Rev. Condens. Matter Phys. **13**, 97–117 (2022).

[13] Guazzelli, E., and O. Pouliquen, "Rheology of dense granular suspensions," J. Fluid Mech. **852**, P1 (2018).

[14] DeGiuli, E., G. Düring, E. Lerner, and M. Wyart, "Unified theory of inertial granular flows and non-Brownian suspensions," Phys. Rev. E **91**, 062206 (2015).

[15] Krieger, I. M., and T. J. Dougherty, "A mechanism for non-Newtonian flow in suspensions of rigid spheres," Trans. Soc. Rheol. **3**, 137–152 (1959).

[16] Otsuki, M., and H. Hayakawa, "Critical scaling near jamming transition for frictional granular particles," Phys. Rev. E **83**, 051301 (2011).

[17] Fernandez, N., R. Mani, D. Rinaldi, D. Kadau, M. Mosquet, H. Lombois-Burger, J. Cayer-Barrioz, H. J. Herrmann, N. D. Spencer, and L. Isa, "Microscopic mechanism for shear thickening of non-Brownian suspensions," Phys. Rev. Lett. **111**, 108301 (2013).

[18] Gallier, S., E. Lemaire, F. Peters, and L. Lobry, "Rheology of sheared suspensions of rough frictional particles," J. Fluid Mech. **757**, 514–549 (2014).

[19] Seto, R., R. Mari, J. F. Morris, and M. M. Denn, "Discontinuous shear thickening of frictional hard-sphere suspensions," Phys. Rev. Lett. **111**, 218301 (2013).

[20] Chèvremont, W., B. Chareyre, and H. Bodiguel, "Quantitative study of the rheology of frictional suspensions: Influence of friction coefficient in a large range of viscous numbers," Phys. Rev. Fluids **4**, 064302 (2019).

[21] Comtet, J., G. Chatté, A. Niguès, L. Bocquet, A. Siria, and A. Colin, "Pairwise frictional profile between particles determines discontinuous shear thickening transition in non-colloidal suspensions," Nat. Commun. **8**, 15633 (2017).

[22] Lobry, L., E. Lemaire, F. Blanc, S. Gallier, and F. Peters, "Shear thinning in non-Brownian suspensions explained by variable friction between particles," J. Fluid Mech. **860**, 682–710 (2019).

[23] Hsiao, L. C., S. Jamali, E. Glynos, P. F. Green, R. G. Larson, and M. J. Solomon, "Rheological state diagrams for rough colloids in shear flow," Phys. Rev. Lett. **119**, 158001 (2017).

[24] Richards, J. A., B. M. Guy, E. Blanco, M. Hermes, G. Poy, and W. C. K. Poon, "The role of friction in the yielding of adhesive 'Brownian' suspensions," J. Rheol. **64**, 405–412 (2020).

[25] Papadopoulou, A., J. J. Gillissen, H. J. Wilson, M. K. Tiwari, and S. Balabani, "On the shear thinning of non-Brownian suspensions:

Friction or adhesion?" J. Non-Newtonian Fluid Mech. **281**, 104298 (2020).

[26] Singh, A., "Hidden hierarchy in the rheology of dense suspensions," MRS Commun. **13**, 971–979 (2023).

[27] Etcheverry, B., Y. Forterre, and B. Metzger, "Capillary-stress controlled rheometer reveals the dual rheology of shear-thickening suspensions," Phys. Rev. X **13**, 011024 (2023).

[28] Clavaud, C., A. Bérut, B. Metzger, and Y. Forterre, "Revealing the frictional transition in shear-thickening suspensions," Proc. Natl. Acad. Sci. U.S.A. **114**, 5147–5152 (2017).

[29] Olsson, P., and S. Teitel, "Herschel-Bulkley shearing rheology near the athermal jamming transition," Phys. Rev. Lett. **109**, 108001 (2012).

[30] Olsson, P., and S. Teitel, "Critical scaling of shear viscosity at the jamming transition," Phys. Rev. Lett. **99**, 178001 (2007).

[31] Jamshidi, R., P. Angeli, and L. Mazzei, "On the closure problem of the effective stress in the Eulerian-Eulerian and mixture modeling approaches for the simulation of liquid-particle suspensions," Phys. Fluids **31**, 013302 (2019).

[32] Buyevich, Y. A., "Particulate stresses in dense disperse flow," Ind. Eng. Chem. Res. **38**, 731–743 (1999).

[33] Hwang, G., and H. Shen, "Modeling the solid phase stress in a fluid-solid mixture," Int. J. Multiphase Flow **15**, 257–268 (1989).

[34] Einstein, A., "Eine neue Bestimmung der Moleküldimensionen," Ann. Phys. **324**, 289–306 (1906).

[35] Jackson, R., *The Dynamics of Fluidized Particles*, Cambridge Monographs on Mechanics (Cambridge University, Cambridge, 2000).

[36] Mazzei, L., Recent advances in modeling gas-particle flows, in *Handbook of Multiphase Flow Science and Technology*, edited by G. H. Yeoh (Springer Singapore, Singapore, 2017), pp. 1–43.

[37] Jeffrey, D. J., and Y. Onishi, "Calculation of the resistance and mobility functions for two unequal rigid spheres in low-reynolds-number flow," J. Fluid Mech. **139**, 261–290 (1984).

[38] Jeffrey, D. J., "The calculation of the low Reynolds number resistance functions for two unequal spheres," Phys. Fluids A: Fluid Dyn. **4**, 16–29 (1992).

[39] Di Felice, R., "The voidage function for fluid-particle interaction systems," Int. J. Multiphase Flow **20**, 153–159 (1994).

[40] Mazzei, L., Eulerian modelling and computational fluid dynamics simulation of mono and polydisperse fluidized suspensions, Ph.D. thesis, University College London, London, 2008. copyright—Database copyright ProQuest LLC; ProQuest does not claim copyright in the individual underlying works; Last updated—2023-02-23.

[41] Liu, Y., Z.-Y. Yin, L. Wang, and Y. Hong, "A coupled CFD–DEM investigation of internal erosion considering suspension flow," Can. Geotech. J. **58**, 1411–1425 (2021).

[42] Bnà, S., R. Ponzini, M. Cestari, C. Cavazzoni, C. Cottini, and A. Benassi, "Investigation of particle dynamics and classification mechanism in a spiral jet mill through computational fluid dynamics and discrete element methods," Powder Technol. **364**, 746–773 (2020).

[43] Cundall, P. D., and O. D. L. Strack, "A discrete numerical model for granular assemblies," Geotechnique **29**, 47–65 (1979).

[44] Horn, R. G., "Surface forces and their action in ceramic materials," J. Am. Ceram. Soc. **73**, 1117–1135 (1990).

[45] Mewis, J., and N. J. Wagner, *Hydrodynamic Effects: Non-Colloidal Particles* (Cambridge University, Cambridge, 2011), pp. 36–79.

[46] Chatté, G., J. Comtet, A. Niguès, L. Bocquet, A. Siria, G. Ducouret, F. Lequeux, N. Lenoir, G. Ovarlez, and A. Colin, "Shear thinning in non-Brownian suspensions," Soft Matter **14**, 879–893 (2018).

[47] Joseph, D., D. Saville, T. Lundgren, and R. Jackson, "Ensemble averaged and mixture theory equations for incompressible fluid-particle suspensions," Int. J. Multiphase Flow **16**, 35–42 (1990).

[48] Mueller, S., E. W. Llewellin, and H. M. Mader, "The rheology of suspensions of solid particles," Proc. R. Soc. A **466**, 1201–1228 (2010).

[49] Batchelor, G. K., and J. T. Green, "The determination of the bulk stress in a suspension of spherical particles to order c^2," J. Fluid Mech. **56**, 401–427 (1972).

[50] Bedeaux, D., "The effective viscosity for a suspension of spheres," J. Colloid Interface Sci. **118**, 80–86 (1987).

[51] O'Hern, C. S., L. E. Silbert, A. J. Liu, and S. R. Nagel, "Jamming at zero temperature and zero applied stress: The epitome of disorder," Phys. Rev. E **68**, 011306 (2003).

[52] Blais, B., M. Lassaigne, C. Goniva, L. Fradette, and F. Bertrand, "Development of an unresolved CFD–DEM model for the flow of viscous suspensions and its application to solid–liquid mixing," J. Comput. Phys. **318**, 201–221 (2016).

[53] Stickel, J. J., and R. L. Powell, "Fluid mechanics and rheology of dense suspensions," Annu. Rev. Fluid Mech. **37**, 129–149 (2005).

[54] Kuznetsov, A. V., "Fluid flow and heat transfer analysis of Couette flow in a composite duct," Acta Mech. **140**, 163–170 (2000).

[55] Boyer, F. M. C., E. Guazzelli, and O. Pouliquen, "Unifying suspension and granular rheology," Phys. Rev. Lett. **107**, 188301 (2011).

[56] Ness, C., and J. Sun, "Flow regime transitions in dense non-Brownian suspensions: Rheology, microstructural characterization, and constitutive modeling," Phys. Rev. E **91**, 012201 (2015).

[57] Zarraga, I., D. Hill, and D. Leighton, "Normal stresses and free surface deformation in concentrated suspensions of noncolloidal spheres in a viscoelastic fluid," J. Rheol. **45**, 1065–1084 (2001).

[58] Sierou, A., and J. F. Brady, "Rheology and microstructure in concentrated noncolloidal suspensions," J. Rheol. **46**, 1031–1056 (2002).

[59] Belytschko, T., *An Overview of Semidiscretization and Time Integration Procedures* (North Holland, Amsterdam, Netherlands, 1983).

[60] Peng, D., S. J. Burns, and K. J. Hanley, "Critical time step for discrete element method simulations of convex particles with central symmetry," Int. J. Numer. Methods Eng. **122**, 919–933 (2021).

[61] Brown, E., and H. M. Jaeger, "Shear thickening in concentrated suspensions: Phenomenology, mechanisms and relations to jamming," Rep. Prog. Phys. **77**, 046602 (2014).

[62] Mazzei, L., and P. Lettieri, "A drag force closure for uniformly dispersed fluidized suspensions," Chem. Eng. Sci. **62**, 6129–6142 (2007).